Computational Materials Science 127 (2017) 141–160

Contents lists available at ScienceDirect

Computational Materials Science

journal homepage: www.elsevier.com/locate/commatsci

# Reliable Molecular Dynamics: Uncertainty quantification using interval analysis in molecular dynamics simulation

Anh V. Tran, Yan Wang *

*Woodruff School of Mechanical Engineering, Georgia Institute of Technology, Atlanta, GA 30332, USA*

ARTICLE INFO

*Article history:*
Received 10 May 2016
Received in revised form 16 September 2016
Accepted 14 October 2016

*Keywords:*
Molecular dynamics
Interatomic potential
Uncertainty quantification
Interval analysis

ABSTRACT

In molecular dynamics (MD) simulation, atomic interaction is characterized by the interatomic potential as the input of simulation models. The interatomic potentials are derived experimentally or from first principles calculations. Therefore they are inherently imprecise because of the measurement error or model-form error. In this work, a Reliable Molecular Dynamics (R-MD) mechanism is developed to extend the predictive capability of MD given the input uncertainty. In R-MD, the locations and velocities of particles are not assumed to be precisely known as in traditional MD. Instead, they are represented as intervals in order to capture the input uncertainty associated with the atomistic model. The advantage of the new mechanism is the significant reduction of computational cost from traditional sensitivity analysis when assessing the effects of input uncertainty. A formalism of generalized interval is incorporated in R-MD, as an intrusive uncertainty quantification method, to model the propagation of uncertainty during the simulation. Error generating functions associated with embedded atomic method (EAM) interatomic potentials are developed to capture the bounds of input variations to demonstrate interval interatomic potentials. Four different uncertainty propagation schemes are proposed to capture the uncertainty of the output. An example of uniaxial tensile loading of single-crystal aluminum is used to demonstrate the R-MD mechanism.



## 1. Introduction

Modeling and simulation tools are crucial for engineers to design and develop new materials efficiently. Uncertainty is always involved in model selection, calibration, and validation processes. Reliable simulation predictions require us to quantify input uncertainty of models. There are two elements of uncertainty in modeling and simulation: aleatory uncertainty and epistemic uncertainty. Aleatory uncertainty is the inherent randomness in the phenomenon being observed, and the impossibility of exhausting all descriptions deterministically. Epistemic uncertainty can be generally related to the lack of perfect knowledge about the involved physical processes [1].

Molecular dynamics (MD) is one of the most widely used atomistic simulation tools. In MD simulation, the aleatory uncertainty corresponds to any fluctuation of the simulated system, e.g. the natural thermal fluctuation that can be described by Boltzmann distribution at an equilibrium microscopic state. The epistemic uncertainty includes, but is not limited to, the imprecise interatomic potentials, the finite size effect, the boundary condition imposed on the simulation cell, and the cutoff radius of the interatomic potentials. The aleatory uncertainty associated with the thermal fluctuation is generally inseparable from MD simulation, and sometimes is induced by the ensemble integrator. For example, in Langevin thermostat, this thermal fluctuation is accounted by the friction-noise in the stochastic differential equations [2]. The epistemic uncertainty in MD simulations is mostly caused by the imperfection of the interatomic potential. These interatomic potentials are typically derived from first principles calculations or approximated based on experimental data. These results are contaminated by both systematic and random errors. The systematic errors of first principles calculations come from different approximations and assumptions in the models, such as Born-Oppenheimer approximation, Hartree-Fock approximation, and the assumed finite linear combination of the variational solution based on the set of basis functions [3]. On the other hand, the systematic errors of experimental results involve measurement bias and calibration errors. Based on the results, an interatomic potential model is formulated with a set of parameters to minimize a measurable error, which usually in turn is converted to a least-square error problem. Because of the non-negative residual in curve fitting and approximation error techniques used in deriving

* Corresponding author.
*E-mail addresses:* yan.wang@me.gatech.edu, prof.yan.wang@gmail.com (Y. Wang).

http://dx.doi.org/10.1016/j.commatsci.2016.10.021
0927-0256/

the interatomic potentials, MD simulations include both model-form uncertainty and parameter uncertainty. Furthermore, the epistemic uncertainty from interatomic potential in MD simulations is amplified because the number of interacting pairs, which scales at least as $N^2$, where $N$ is the number of atoms. Therefore, quantifying uncertainty in MD simulations is a critical problem, in both assessing the accuracy and reliability of the simulation prediction.

Uncertainty quantification (UQ) problems are divided into two main paradigms, intrusive and non-intrusive methods on probabilistic and non-probabilistic frameworks. In non-intrusive UQ techniques, the simulation is viewed as a black box, and the simulator is modeled as a one-to-one non-linear function that maps from the input domains to the output or quantities of interests. Popular techniques, including stochastic collocation, Monte Carlo, and global sensitivity analysis, rely on statistical techniques to build comprehensive output distributions based on the assumed input distributions. Generalized polynomial chaos expansion is a widely used technique, and can be utilized either intrusively or non-intrusively. As an intrusive technique, it has been applied to solve stochastic differential equations and partial differential equations with random inputs. As a non-intrusive technique, it is typically used together with Smolyak sparse grid and nested sets in stochastic collocation methods.

Other intrusive UQ techniques, such as local sensitivity analysis and interval-based approaches, aim to provide the output probability density function or its bounded support for expensive simulation by incorporating and propagating the uncertainty *internally* using minimal number of runs. In interval-based approaches, the uncertainty is coupled into the input and represented by intervals. The simulator is thus extended to handle the interval inputs and propagate the uncertainty throughout the simulation. The output uncertainty, which is also represented as intervals, is computed at every time step at a relatively cheap computational cost.

Various UQ methods have been applied to multi-scale simulation for materials. Comprehensive literature reviews are available in [4,5]. Frederiksen and Jacobsen [6] applied Bayesian update to train the interatomic potentials parameters with experimental data sets by minimizing the square error between experimental data and simulation results. Jacobson et al. [7] constructed response surfaces with Lagrange interpolation to study the sensitivity of macroscopic properties with respect to interatomic potential parameters. Cailliez and Pernot [8] calibrated Lennard-Jones potential for Argon based on Bayesian calibration/prediction framework. Rizzi et al. [9,10] assumed uniform distribution for the four-site, TIP4P, water model parameters and constructed the generalized polynomial chaos representation by non-intrusive spectral projection and Bayesian inference approaches, then later on, calibrated these force-field parameters based on Bayesian inference. Angelikopoulos et al. [11] applied the Bayesian calibration to calibrate the water-carbon interactions based on water contact angles in water wetting of graphene, the aggregation of fullerenes in aqueous solution, and the water transport across carbon nanotubes. Rizzi et al. [9] applied polynomial chaos expansion to study the effect of input uncertainty in MD. Cailliezf et al. [12] applied the efficient global optimization algorithms in parameter space to calibrate the potential parameters for TIP4P model, based on probabilistic kriging metamodels. Wen et al. [13] studied the effect of different spline interpolations on the potential predictions by calculating the quasi-harmonic thermal expansion and finite-temperature elastic constant of a one-dimensional chain in tabulated interatomic potentials. Hunt et al. [14] developed a software package for non-intrusive propagation of uncertainties in input parameters, using surrogate models and adaptive sampling methods, such as Monte Carlo, Latin Hypercube, and Smolyak sparse grids, based on generalized polynomial chaos expansion. Li et al. [15] discussed the cut- and random sample-high dimensional model representation to quantify the uncertainty induced by potential surfaces.

As an intrusive approach on non-probabilistic framework, we recently proposed an interval-based reliable MD (R-MD) mechanism [16,17] that incorporates Kaucher interval arithmetic [18] into classical MD to quantify output uncertainty. Classical interval arithmetic provides a complete solution by capturing all possibilities for simple algebraic operations, such as addition, subtraction, multiplication, and division. Kaucher interval arithmetic generalizes and extends [19] classical interval arithmetic with better topology and algebraic properties. Compared to classic interval arithmetic, Kaucher interval arithmetic is preferred for three reasons. Firstly, the over-estimation problem is significantly reduced. Secondly, the self-dependency problem, which also results in an over-estimation of a function, where dependent variables are repeated more than once, is mitigated. Thirdly, the negation and reciprocal operations with respect to addition and multiplication exist. In contrast to the Kaucher interval space, the classical interval space only forms a semi-group algebraic structure because of the lack of invertibility. In R-MD, the input uncertainty associated with interatomic potentials is captured in interval forms, either as intervals or as interval functions. Consequently, the atomistic positions, velocities, and forces are also interval-valued. Fig. 1 plots a schematic sketch of simple 2D R-MD simulation cell, where the atomistic positions are interval-valued. The exact atomistic positions and velocities are unknown, but bounded by intervals. In this paper, the details of how Kaucher interval arithmetic is applied in simulation including interval potential, interval force computation, and interval statistical ensemble are described. In Section 2, we review the algebraic operations of Kaucher interval arithmetic. In Section 3, the formulation of interval potential and interval force are discussed, and four R-MD uncertainty propagation schemes are implemented in the framework of Large-scale Atomic/Molecular Massively Parallel Simulator, also known as LAMMPS [20]. An application to tensile uniaxial deformation of aluminum single crystal is demonstrated in Section 4, including UQ results, comparisons between different schemes, finite-size effects, and comparison with sensitivity analysis results as a part of verification process. Following are the discussion in Section 5 and conclusion in Section 6.

## 2. Kaucher interval arithmetic

The classical interval space, denoted as $\mathbb{IR}$, is a collection of classical interval, where the upper bound is strictly greater than or

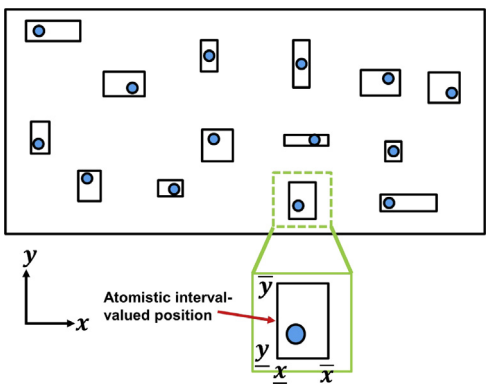


**Fig. 1.** Schematic illustration of R-MD in 2D.

equal to the lower bound, that is, $\overline{x} \geqslant \underline{x}$. The Kaucher interval space is a collection of Kaucher intervals, denoted as $\mathbb{KR}$, is an extension of classical interval space $\mathbb{IR}$, where the aforementioned constraint of upper and lower bounds is removed. The dual operator simply swaps the lower and the upper bounds of an arbitrary interval simultaneously, as dual $[\underline{x},\overline{x}] := [\overline{x},\underline{x}]$. In order to distinguish arithmetic operation on $\mathbb{KR}$ to $\mathbb{IR}$, the addition, subtraction, multiplication, and division operator are denoted with a circumscribed operator, and defined as follows. $[\underline{x},\overline{x}] \oplus \left[\underline{y},\overline{y}\right] = \left[\underline{x}+\underline{y},\overline{x}+\overline{y}\right]$. $[\underline{x},\overline{x}] \ominus \in \left[\underline{x}-\underline{y},\overline{x}-\overline{y}\right]$. $[\underline{x},\overline{x}] \otimes \left[\underline{y},\overline{y}\right]$ is defined in Table 1. $[\underline{x},\overline{x}] \oslash \left[\underline{y},\overline{y}\right] = [\underline{x},\overline{x}] \otimes \left[1/\overline{y}, 1/\underline{y}\right]$. In Table 1, the generalized interval space $\mathbb{KR}$ is decomposed into four subspaces: $\mathcal{P} := \{\boldsymbol{x} \in \mathbb{KR} \mid \underline{\boldsymbol{x}} \geqslant 0,\ \overline{\boldsymbol{x}} \geqslant 0\}$ contains positive intervals, $\mathcal{Z} := \{\boldsymbol{x} \in \mathbb{KR} \mid \underline{\boldsymbol{x}} \leqslant 0 \leqslant \overline{\boldsymbol{x}}\}$ contains proper interval that include zero, $-\mathcal{P} := \{\boldsymbol{x} \in \mathbb{KR} \mid -\boldsymbol{x} \in \mathbb{P}\}$ contains negative intervals, and dual $\mathcal{Z} := \{\boldsymbol{x} \in \mathbb{KR} \mid \text{dual } \boldsymbol{x} \in \mathcal{Z}\}$contains improper intervals that include zero.

Let $x^+ = \max\{x, 0\}$, $x^- = \max\{-x, 0\}$, $x \vee y = \max\{x, y\}$, the multiplication table can be further simplified by Lakeyev's formula [21] as

$$[\underline{x},\overline{x}] \cdot \left[\underline{y},\overline{y}\right] = \left[(\underline{x}^+\underline{y}^+) \vee (\overline{x}^-\overline{y}^-) - (\overline{x}^+\underline{y}_-) \vee (\underline{x}^-\overline{y}^+), (\overline{x}^+\overline{y}^+) \vee (\underline{x}^-\underline{y}^-) - (\underline{x}^+\overline{y}^-) \vee (\overline{x}^-\underline{y}^+)\right] \quad (1)$$

The Kaucher interval space $\mathbb{KR}$ is equipped with a norm defined as

$$\|\boldsymbol{x}\| := \max\{|\underline{x}|, |\overline{x}|\} \quad (2)$$

with the following properties:

$\|\boldsymbol{x}\| = 0$ if and only if $\boldsymbol{x} = 0$ (separates points),
$\|\boldsymbol{x}+\boldsymbol{y}\| \leqslant \|\boldsymbol{x}\| + \|\boldsymbol{y}\|$ (subadditivity or triangle inequality),
$\|\alpha\boldsymbol{x}\| = |\alpha|\|\boldsymbol{x}\|$ with $\alpha \in \mathbb{R}$ (absolute homogeneity).

A induced distance metric on $\mathbb{KR}$ is then can be defined as an extension of norm between $\boldsymbol{x}$ and $\boldsymbol{y}$ as

$$d(\boldsymbol{x},\boldsymbol{y}) := \max\left\{|\underline{x}-\underline{y}|, |\overline{x}-\overline{y}|\right\}, \quad (3)$$

which is related with the norm by $d(\boldsymbol{x}, 0) = \|\boldsymbol{x}\|$ and $d(\boldsymbol{x},\boldsymbol{y}) = \|\boldsymbol{x} \ominus \boldsymbol{y}\|$. As shown in [18], $\mathbb{KR}$ is a complete metric space under the defined metrics $d(\cdot,\cdot)$.

**Definition 1.** An interval $\boldsymbol{x}$ is *proper* if the upper bound is greater than or equal to the lower bound, that is, $\underline{x} \leqslant \overline{x}$. An interval and called *improper* if that lower bound is greater than or equal to the upper bound, that is, $\underline{x} \geqslant \overline{x}$. If two bounds equal each other, $\underline{x} = \overline{x}$, then $\boldsymbol{x}$ is a *degenerated*, *pointwise* or *singleton* interval, and has a real value.

**Definition 2.** An interval is called *sound* if it does not include inadmissible solutions; an interval solution is called *complete* if it includes all possible solutions. In general, a sound interval is a subset of the true solution set, whereas a complete interval is a superset.

**Table 1**
Definition of Kaucher multiplication.

| | $\boldsymbol{y} \in \mathcal{P}$ | $\boldsymbol{y} \in \mathcal{Z}$ | $\boldsymbol{y} \in -\mathcal{P}$ | $\boldsymbol{y} \in$ dual $\mathcal{Z}$ |
|---|---|---|---|---|
| $\boldsymbol{x} \in \mathcal{P}$ | $\left[\underline{xy}, \overline{xy}\right]$ | $\left[\overline{x}\underline{y}, \overline{xy}\right]$ | $\left[\overline{x}\underline{y}, \underline{x}\overline{y}\right]$ | $\left[\underline{xy}, \underline{x}\overline{y}\right]$ |
| $\boldsymbol{x} \in \mathcal{Z}$ | $[\underline{x}\overline{y}, \overline{xy}]$ | $\left[\min\left\{\underline{x}\overline{y}, \overline{x}\underline{y}\right\}, \max\left\{\underline{xy}, \overline{xy}\right\}\right]$ | $\left[\overline{x}\underline{y}, \underline{xy}\right]$ | 0 |
| $\boldsymbol{x} \in -\mathcal{P}$ | $\left[\underline{x}\overline{y}, \overline{x}\underline{y}\right]$ | $\left[\underline{x}\overline{y}, \underline{xy}\right]$ | $\left[\overline{xy}, \underline{xy}\right]$ | $\left[\overline{xy}, \overline{x}\underline{y}\right]$ |
| $\boldsymbol{x} \in$ dual$\mathcal{Z}$ | $\left[\underline{xy}, \overline{x}\underline{y}\right]$ | 0 | $[\overline{xy}, \underline{x}\overline{y}]$ | $\left[\max\left\{\underline{xy}, \overline{xy}\right\}, \min\left\{\underline{x}\overline{y}, \overline{x}\underline{y}\right\}\right]$ |

## 3. Reliable Molecular Dynamics (R-MD)

Using Kaucher intervals, R-MD incorporates the input uncertainties in the interatomic potential with the interval forms. The sensitivity of the interested quantities with respect to inputs is assessed on-the-fly at every time step. Compared to the non-intrusive solutions, the intrusive UQ techniques significantly reduce the computational time to estimate the uncertainty of the output.

### 3.1. Representations of atoms' position, velocity and forces intervals

There are mainly two ways to represent an interval $\boldsymbol{x} = [\underline{x},\overline{x}]$, either as upper bound $\overline{x}$ and lower bound $\underline{x}$, or midpoint $\text{mid}(\boldsymbol{x}) = \frac{1}{2}(\overline{x}+\underline{x})$ and radius $\text{rad}(\boldsymbol{x}) = \frac{1}{2}(\overline{x}-\underline{x})$. The advantage of the lower-upper bounds representation is that the computational time is optimized, because most of the interval calculations are performed under this representation. However, it would require heavy modifications to incorporate the intervals into MD simulation. On the other hand, the midpoint-radius representation can be built as a simple extension based on the classical MD packages. The midpoint values of atoms' interval positions, velocities, and forces intervals can be assigned as the values in classical MD at every time step, and the radii can be computed based on the lower or upper bounds accordingly. With the radii of the interval positions, velocities, and forces, the uncertainty of the quantities of interest can be quantified accordingly. The drawback of this technique is that it is not computationally optimal because of the repetitive converting processes to lower-upper bounds representation.

A caveat for midpoint-radius representation is the over-constraint problem of choosing radius values for atoms' interval positions, velocities, and forces. This problem is described in Fig. 2a. Because the values from classical MD are not necessarily the exact midpoint, two radii are differentiated. One is inner radius, the other is outer radius. The inner radius is the smaller distance from midpoint to one of the interval bounds, whereas the outer radius is the larger distance. If the inner radius is chosen, the interval is sound and the solution underestimates the true uncertainties. If the outer radius is chosen, the interval is complete and the solution over-estimates the true uncertainties. In the inner radius case, the soundness is chosen over the completeness. In the outer radius case, the completeness is chosen over the soundness. Based on the introduction of radius variable, Fig. 2b presents the possibility of decoupling radius variables from the interval variables for the atomistic positions, velocities, and forces. This is an advantage of the midpoint-radius representation because instead of building interval objects to handle, the decoupling allows the direct calculation of the radius variable, which in turns can be used to quantify the uncertainty of the output.

### 3.2. Interval interatomic potential

The interatomic potentials are approximated based on physical models and therefore they are inherently imprecise due to approximation errors. Typically, the model and its parameters are chosen

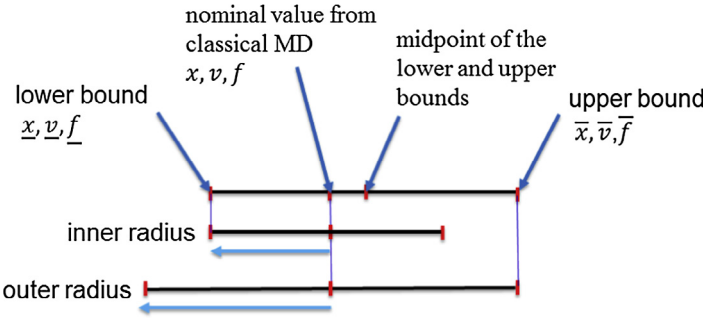


(a) The over-constraint problem by the choice of inner and outer radius in midpoint-radius representations of an interval.

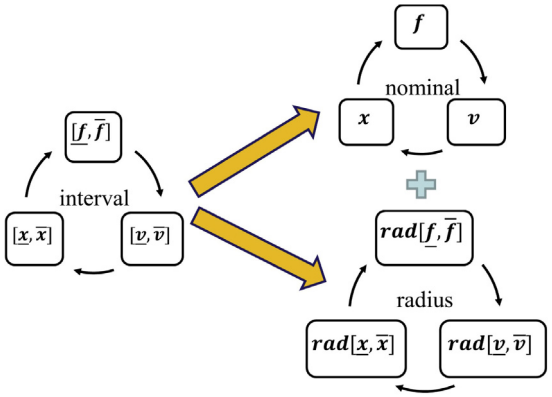


(b) The decoupling technique to accelerate computation in midpoint-radius representation.

**Fig. 2.** Illustration of (a) the relationship between inner-outer radius with sound-complete solution and (b) decoupling of radius values in R-MD.

to fit for a particular purpose using curve fitting techniques, or multi-linear regression analysis to minimize the residue, or maximum likelihood estimator, associated with the interested output quantities. In MD, these quantities are usually lattice constant, phonon-dispersion curve, stacking fault energy, melting point temperature, thermoelastic properties, as well as other mechanical and thermal properties of a material.

In R-MD, interval-valued interatomic potentials are applied to model the input uncertainty. For example, for Lennard-Jones potential, the well depth $\varepsilon$ and the location at which the interatomic potential between two atoms is zero $\sigma$ can be generalized as $[\underline{\varepsilon}, \overline{\varepsilon}]$ and $[\underline{\sigma}, \overline{\sigma}]$. For tabulated potentials such as embedded atomic model (EAM), some analytical error generating functions can be devised to represent the error bounds of potentials and the interpolation error of the potentials. With interval-valued interatomic potentials, the forces are also intervals. The update of positions and velocities is based on Kaucher interval arithmetic, which is described in Section 2.

### 3.3. Interval force calculations

The force computation plays a pivotal role in R-MD. Theoretically, it is a simplification of a NP-problem. Consider a 2D R-MD simulation, where an arbitrary atom has $N$ neighboring atoms, as sketched in Fig. 3a. Mathematically, the interval force can be computed rigorously by considering the interaction between vertices of each individual rectangles, as illustrated in Fig. 3b. For 2D, in one neighboring list, this approach leads to $4^N$ possibilities to compute a total resulting force for one atom at every time step, and thus very exhaustive. The problem is worse in R-MD 3D, because the number of possibilities increases to $8^N$. Without approximations and simplifications, this problem leads to an exhaustive search to find a good estimation of interval forces. To simplify, the interatomic forces are computed based on the centroids of the prisms with weak-strong variation assumptions. This statement will be explained in further details for EAM potential in the next section.

#### 3.3.1. An example of interval-valued potential: Interval EAM potential

In this section, our previous work in [16] to introduce uncertainty in EAM potentials is summarized. The EAM is a semi-empirical, many-atom potential and well suited for metallic systems. Instead of solving the many-electron Schrödinger equation, the total energy of a solid at any atomic arrangements can be calculated based on the local-density approximation. This approximation views the energy of the metal as the energy obtained by embedding an atom into the local electron density provided by the remaining atoms of the system. In addition, there is an electrostatic interaction, which is the two-body term. Each atom can be viewed as an impurity in the host of other atoms, and when an impurity is introduced, the total potential is a sum of host and impurity potentials. Daw and Baskes [22,23], following Stott-Zaremba corollary, proposed an approximation to the total potential as

$$E_{tot} = \sum_i F(\rho_i) + \frac{1}{2}\sum_{\substack{ij \\ i \neq j}} \phi(r_{ij}) \tag{4}$$

$\phi(r_{ij})$ is the short-range *pairwise potential* describing the electrostatic contribution. $\rho_i$ is the density of the host at the position $r_i$ but without atom $i$. The host density can be further approximated

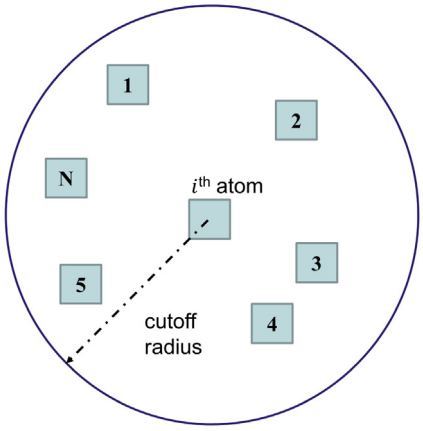


(a) $N$ atom in a neighboring list

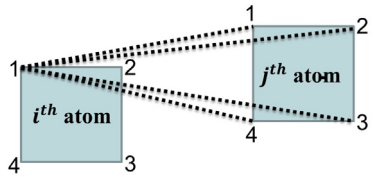


(b) Interaction between one vertex with other vertices in another prism in R-MD

**Fig. 3.** 2D R-MD force simplification problem.

by a sum of the atomic density $f$ of the constituents as $\rho_i = \sum_{j\neq i} f_j(r_{ij})$, where $f_j$, the *local density function*, is a simple function of the position of other atoms positions. $F$ is the *embedding energy function*, which is the energy to place an atom in the electron environment at the local electron density $\rho_i$.

In the R-MD mechanism, the interatomic potential uncertainty is modeled by two forms of error generating functions, $e_1(r_{ij})$ and $e_2(\rho)$, which are associated with $\rho(r_{ij})$ or $\phi(r_{ij})$, and $F(\rho)$, respectively, depending on whether the function's domain is the electron density $\rho$ or the interatomic distance $r$. The interval electron density function is $\left[\underline{\rho},\overline{\rho}\right](r_{ij}) = \rho(r_{ij}) \pm e_1^{(\rho)}(r_{ij})$, the interval pairwise potential is $\left[\underline{\phi},\overline{\phi}\right](r_{ij}) = \phi(r_{ij}) \pm e_1^{(\phi)}(r_{ij})$, and the interval embedding energy function is $\left[\underline{F},\overline{F}\right](\rho) = F(\rho) \pm e_2^{(F)}(\rho)$. We refer to $e_1(r)$ as type I error generating function which associates with $r$ domain, and $e_2(\rho)$ as type II error generating function which associates with $\rho$ domain. As the interatomic distance between two atom $i$ and $j$ $r_{ij} \to \infty$, their interaction becomes weaker and approach to 0 asymptotically. On the other hand, the electron density function $\rho(r_{ij})$ and the pairwise potential $\phi(r_{ij})$ of $r_{ij}$ must remain bounded as $r_{ij} \to 0$. In addition, the inclusion properties of interval must be kept for both the original functions and their first derivatives. Consequently, the type I error generating function $e_1(r)$ is required to satisfy the following six conditions. The error function and its first derivative must be bounded in the vicinity of zero, i.e., (1) $\lim_{r\to 0} e_1(r) < \infty$ and (2) $\lim_{r\to 0} \frac{\partial e_1(r)}{\partial r} < \infty$. The function and its first derivative must decay asymptotically, i.e., (3) $\lim_{r\to\infty} e_1(r) = 0$ and (4) $\lim_{r\to\infty} \frac{\partial e_1(r)}{\partial r} = 0$. The value of the function and its derivative must be included in the interval, i.e., (5) $\forall r \in [0,\infty) : f(r) \in [f(r) \pm e_1(r)]$ and (6) $\frac{\partial f(r)}{\partial r} \in \left[\frac{\partial \rho(r) \pm \partial e_1(r)}{\partial r}\right]$, where $f(r)$ denotes the function either $\rho(r_{ij})$ or $\phi(r_{ij})$. Based on the six required conditions, two analytical and admissible forms are found. They are a rational function where the denominator is one degree higher than the numerator as

$$e_1(r) = \frac{a_1 r + a_0}{b_2 r^2 + b_1 r + b_0} \tag{5}$$

and an exponential function as

$$e_1(r) = a e^{-br} \quad \text{where } b > 0. \tag{6}$$

Similarly, the analytical choice of type II error generating function associated with $F(\rho)$ is limited by five conditions. (1) The error function must have a negative finite slope at $\rho = 0$ for $F(\rho) \pm e_2(\rho)$, i.e. $-\infty < \frac{\partial [F(\rho) \pm e_2(\rho)]}{\partial \rho} < 0$. (2) The function must have a positive slope at large electron density for $F(\rho) \pm e_2(\rho)$. (3) The function must decay asymptotically when two atoms are far away, i.e. $\lim_{\rho\to\infty} e_2(\rho) = 0$. (4) The function must be non-negative function, i.e., $e_2(\rho) \geqslant 0, \forall \rho \in [0,\infty)$. (5) The local extrema (in this case, *maxima*) at $\rho = \rho_0$ because $F(\rho) \pm e_2(\rho)$ attains its minimum $\rho_0$ as well, thus $\frac{\partial [F(\rho) \pm e_2(\rho)]}{\partial \rho}|_{\rho=\rho_0} = 0$ means that $\frac{\partial e_2(\rho)}{\partial \rho}|_{\rho=\rho_0} = 0$. The condition (5) corresponds to the so-called effective pair scheme, which requires the embedding function to attain its minimum at the density of equilibrium crystal [24]. One analytical choice of the error generating function of type II that satisfies all of these conditions is

$$e_2(\rho) = a\left(\frac{\rho}{\rho_0}\right)^{b\rho_0} e^{-b(\rho-\rho_0)}, \quad b > \frac{1}{\rho_0}, \quad b\rho_0 \notin \{0,1\}. \tag{7}$$

For EAM potential, the classical force for atom $i$th based on its neighborhood ($j$th atoms) is calculated as

$$\vec{\boldsymbol{F}}_i = -\sum_{j\neq i}\left[\left.\frac{\partial F_i(\rho)}{\partial \rho}\right|_{\rho=\rho_i} \cdot \left.\frac{\partial \rho_j(r)}{\partial r}\right|_{r=r_{ij}} + \left.\frac{\partial F_j(\rho)}{\partial \rho}\right|_{\rho=\rho_j} \cdot \left.\frac{\partial \rho_i(r)}{\partial r}\right|_{r=r_{ij}} + \left.\frac{\partial \phi_{ij}(r)}{\partial r}\right|_{r=r_{ij}}\right] \frac{\left(\vec{\boldsymbol{r}}_i - \vec{\boldsymbol{r}}_j\right)}{r_{ij}} \tag{8}$$

where $\vec{\boldsymbol{F}}$ is the vector force, $F(\rho)$ is the embedding energy, $\rho(r)$ is the local electron density function, $\phi(r_{ij})$ is the pairwise potential. For interval EAM potential, the upper and lower bounds of the interval force are extended based on the classical force calculation and calculated separately as

$$\begin{aligned}\vec{\underline{\boldsymbol{F}}}_i = -\sum_{j\neq i}\Bigg[&\left(\left.\frac{\partial F_i(\rho)}{\partial \rho}\right|_{\rho=\rho_i} - \left.\frac{\partial\, e_2^{(F)}(\rho)}{\partial \rho}\right|_{\rho=\rho_i}\right) \cdot \left(\left.\frac{\partial \rho_j(r)}{\partial r}\right|_{r=r_{ij}} - \left.\frac{\partial\, e_1^{(\rho)}(r)}{\partial r}\right|_{r=r_{ij}}\right) \\ &+ \left(\left.\frac{\partial F_j(\rho)}{\partial \rho}\right|_{\rho=\rho_j} - \left.\frac{\partial\, e_2^{(F)}(\rho)}{\partial \rho}\right|_{\rho=\rho_j}\right) \cdot \left(\left.\frac{\partial \rho_i(r)}{\partial r}\right|_{r=r_{ij}} \left.\frac{\partial - e_1^{(\rho)}(r)}{\partial r}\right|_{r=r_{ij}}\right) \\ &+ \left(\left.\frac{\partial \phi(r)}{\partial r}\right|_{r=r_{ij}} - \left.\frac{\partial\, e_1^{(\phi)}(r)}{\partial r}\right|_{r=r_{ij}}\right)\Bigg] \cdot \frac{\left(\vec{\underline{\boldsymbol{r}}}_i - \vec{\underline{\boldsymbol{r}}}_j\right)}{r_{ij}}\end{aligned} \tag{9}$$

$$\overrightarrow{\overline{\boldsymbol{F}}}_i = -\sum_{j\neq i}\left[\left(\left.\frac{\partial F_i(\rho)}{\partial \rho}\right|_{\rho=\rho_i} + \left.\frac{\partial\, e_2^{(F)}(\rho)}{\partial \rho}\right|_{\rho=\rho_i}\right)\cdot\left(\left.\frac{\partial \rho_j(r)}{\partial r}\right|_{r=r_{ij}} + \left.\frac{\partial\, e_1^{(\rho)}(r)}{\partial r}\right|_{r=r_{ij}}\right)\left(\left.\frac{\partial F_j(\rho)}{\partial \rho}\right|_{\rho=\rho_j} + \left.\frac{\partial\, e_2^{(F)}(\rho)}{\partial \rho}\right|_{\rho=\rho_j}\right)\cdot\left(\left.\frac{\partial \rho_i(r)}{\partial r}\right|_{r=r_{ij}} + \left.\frac{\partial\, e_1^{(\rho)}(r)}{\partial r}\right|_{r=r_{ij}}\right) + \left(\left.\frac{\partial \phi(r)}{\partial r}\right|_{r=r_{ij}} + \left.\frac{\partial\, e_1^{(\phi)}(r)}{\partial r}\right|_{r=r_{ij}}\right)\right]\cdot\frac{\left(\overrightarrow{\boldsymbol{r}_i} - \overrightarrow{\boldsymbol{r}_j}\right)}{r_{ij}} \tag{10}$$

If the error generating functions are zeros almost everywhere, the interval force converges to the classical force, which is a singleton interval. Fig. 4a illustrates the computation of atomistic interval radius at each time step. The atomic interactions between atom $i$ and its neighbors are assumed to vary within some ranges and become slightly stronger or weaker based on the prescribed interval potential functions. Therefore, the total force acting on atom i at one time step can be captured by an upper bound and a lower bound, or an interval force vector. The upper bound and lower bound of the force interval can have different magnitudes, as well as different directions, as illustrated Fig. 4b. Compared to our previous work [16,17], here the signum function is not included to allow more variations in the interval interatomic forces.

### 3.4. Uncertainty propagation schemes

Four schemes are developed to quantify and propagate the uncertainty. They are termed midpoint-radius, lower–upper bounds, total uncertainty principle, and interval statistical ensemble schemes.

#### 3.4.1. Midpoint-radius scheme

At each time step, the lower and upper bounds of the pairwise interval force can be separately computed according to the interval-valued potentials. Based on the midpoint-radius representation of an arbitrary interval in Kaucher interval space $\mathbb{KR}$, the inner and outer radii of force intervals can be computed respectively as

$$\begin{aligned}\mathrm{rad}_{\mathrm{inner}}\left[\underline{f},\overline{f}\right] &= \begin{cases}\min\left\{\overline{f}-f^*, f^*-\underline{f}\right\}, & \text{if } \left[\underline{f},\overline{f}\right] \text{ is proper}\\ \max\left\{\overline{f}-f^*, f^*-\underline{f}\right\}, & \text{if } \left[\underline{f},\overline{f}\right] \text{ is improper}\end{cases}\\ \mathrm{rad}_{\mathrm{outer}}\left[\underline{f},\overline{f}\right] &= \begin{cases}\max\left\{\overline{f}-f^*, f^*-\underline{f}\right\}, & \text{if } \left[\underline{f},\overline{f}\right] \text{ is proper}\\ \min\left\{\overline{f}-f^*, f^*-\underline{f}\right\}, & \text{if } \left[\underline{f},\overline{f}\right] \text{ is improper}\end{cases}\end{aligned} \tag{11}$$

where $f^*$ denotes the nominal force from traditional MD calculation, $\underline{f}$ and $\overline{f}$ denote the lower and upper bounds of the interval forces, respectively. This formula is consistent with the fact that a proper interval has positive interval radius, and an improper interval has negative interval radius. The radius of pairwise interval force is then computed based on the choice of inner or outer radius. The radius of each pairwise interval force associated with atom $i$ can be summed together within its neighborhood to produce the radius of the total interval force for atom $i$ at one time step. The corresponding radii for atomistic interval velocities and interval positions can then be updated accordingly. At each time step, the midpoint value of pairwise interval force is reassigned as the usual nominal pairwise force value $f^*$ in classical MD simulation, as shown in Fig. 2a. With the radius and midpoint of the atomistic interval forces, velocities, and positions, one can reconstruct the according intervals of atom $i$ at that time step. The advantage of this scheme is that the number of operations can be reduced based on the fact that the midpoint of interval positions and interval velocities are equal to the classical MD values and the calculations of radii and midpoints can be decoupled, as described in Section 3.1. The decoupling process allows for shortening computational time by computing the radii of the atomistic intervals directly. The computational procedure is summarized in Algorithm 1.

One technical issue of the midpoint-radius uncertainty propagation scheme is that the inner radii tend to underestimate the uncertainty of the forces, positions, and velocities, whereas the outer radii tend to over-estimate the uncertainty. Therefore, two runs of simulation, one with inner radii option, the other with outer radii option, are recommended. Although the actual interval bounds are unknown, the results from these two simulation runs can give a good estimate of error bounds. The choice of inner radii is associated with higher soundness, whereas the choice of outer radii is associated with higher completeness, because the solution set is broader in the later case.

A caveat for this implementation scheme is that for isothermal ensemble, such as isothermal-isobaric (NPT) statistical ensemble, the uncertainty associated with temperature is pessimistically large even though the epistemic uncertainty associated with temperature should be small, because it mostly fluctuates around a constant. The temperature is computed by

$$\text{Kinetic Energy} = \sum_{k=1}^{N}\frac{m v_k^2}{2} = \frac{1}{2}dNk_BT \tag{12}$$

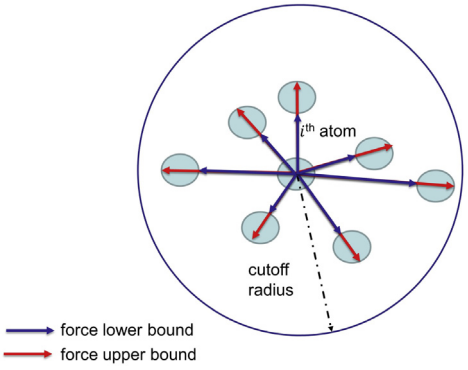


(a) pairwise force between atom $i$ and its neighbors: upper and lower bounds calculation

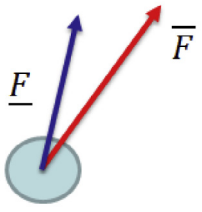


(b) total force acting on atom $i$ at one time step

**Fig. 4.** The computational process of the interval force acting one atom at every time step.

where $N$ is the number of atoms, $k_B$ is the Boltzmann constant, $T$ is the temperature, and $d$ is the dimensionality of the simulation. Because of the over-estimation issue, the uncertainty associated with temperature is set as 0 in this scheme to preserve the isothermal properties of the statistical isothermal-isobaric ensemble, and hence only the uncertainties in atoms' positions and forces contribute to the pressure uncertainty. The output of this scheme is the radii values of the interval output.

**Algorithm 1.** Implementation of midpoint-radius scheme.

**for** every time step **do**
  compute the total upper bound force $\overline{f}$
  compute the total lower bound force $\underline{f}$
  compute the total nominal force $f^*$
  compute the pairwise force interval radius $rad(f)$ based on the choice of inner or outer radius
  $rad(v) \leftarrow rad(v) + rad(f)/m$
  $rad(x) \leftarrow rad(x) + rad(v) \cdot \Delta t$
  quantifying uncertainty by interval radius of atomistic positions, velocities, and forces
**end for**

### 3.4.2. Lower-upper bounds scheme

The second approach to implement R-MD mechanism is to utilize the lower and upper bounds representation of Kaucher intervals to model the uncertainty of each atoms in the MD simulation. Therefore this approach is referred to as lower-upper bounds scheme throughout this work. In this approach, the upper and lower bound values of the atomistic positions, velocities, and forces, as well as their nominal values are retained at every time step. The nominal value of the atomistic interval velocities are updated based on the classical MD, whereas the lower and upper bounds of the atomistic interval velocities are updated from the *nominal* velocities and the lower and upper bounds of the total interval force. In the same manner, the nominal value of the atomistic interval positions are updated based on the nominal value of the atomistic interval velocities, whereas the bounds of the atomistic interval positions are updated according to both the nominal value of the atomistic interval positions and the bounds of the atomistic interval velocities. This computational scheme is described in Algorithm 2 for velocity-Verlet integrators. The output of this scheme is interval outputs, with lower and upper bounds.

**Algorithm 2.** Implementation of lower-upper bounds scheme.

**for** every time step **do**
  compute the total upper bound force $\overline{f}$
  compute the total lower bound force $\underline{f}$
  $v \leftarrow v + f/m$
  $\overline{v} \leftarrow v + \overline{f}/m$
  $\underline{v} \leftarrow v + \underline{f}/m$
  $x \leftarrow x + v \cdot \Delta t$
  $\overline{x} \leftarrow x + \overline{v} \cdot \Delta t$
  $\underline{x} \leftarrow x + \underline{v} \cdot \Delta t$
  compute interval outputs
**end for**

### 3.4.3. Total uncertainty principle scheme

In this computational implementation, besides using the error generating function to quantify the uncertainty in the atomistic total force, the radii of atoms' interval velocities are assumed to be a fixed percentage of the magnitude of velocities. The total uncertainty principle scheme is conceptually equivalent to the temperature scaling process in isothermal-isobaric ensemble by coupling the simulation system to a thermostat. The scheme is based on the so-called total uncertainty principle, which states that the total uncertainty level of the system during two consecutive observations remains the same. As a result, the uncertainty needs to be scaled back from time to time during simulation. The physical meaning of this process is that the temperature of the simulation cell is measured at every time step, so that the total uncertainty of the simulation is roughly at the same scale throughout the system. The scaling process is mathematically expressed as

$$\mathrm{rad}(\boldsymbol{v}) = \alpha\% \cdot v^*, \quad \text{for Kaucher interval subscheme} \tag{13}$$

$$\mathrm{rad}(\boldsymbol{v}) = \alpha\% \cdot |v^*|, \quad \text{for classical interval subscheme} \tag{14}$$

where $v^*$ denotes the classical MD values of the atoms' velocities, which is also the nominal values of the atomistic interval velocities. Eqs. (13) and (14) are associated with Kaucher intervals and classical intervals, respectively. The total uncertainty principle scheme is implemented according to Algorithm 3. The total uncertainty scheme with the strictly non-negative radius of interval velocities, described by Eq. (14), as the total uncertainty scheme *with classical intervals*. The other uncertainty scheme, described by Eq. (13), is referred to as the total uncertainty scheme *with Kaucher intervals*. The total principle uncertainty scheme can be thought as an extension to the midpoint-radius scheme described in Section 3.4.1.

**Algorithm 3.** Implementation of total uncertainty principle scheme.

**for** every time step **do**
  compute the total upper bound force $\overline{f}$
  compute the total lower bound force $\underline{f}$
  compute the total nominal force $f^*$
  compute the pairwise force interval radius $rad(f)$ based on the choice of inner or outer radius
  $rad(v) \leftarrow \alpha\% \cdot v^*$ or $rad(v) \leftarrow \alpha\% \cdot |v^*|$
  $rad(v) \leftarrow rad(v) + rad(f)/m$
  $rad(x) \leftarrow rad(v) \cdot \Delta t$
  quantifying uncertainty by interval radius of atomistic positions, velocities, and forces
**end for**

### 3.4.4. Interval statistical ensemble scheme: interval isothermal-isobaric (NPT) ensemble

As a result of incorporating the uncertainty into each atomistic position, velocity and force, the system control variables also have their own uncertainty and should be consequently modeled as intervals. For example, in NPT ensemble, the pressure and temperature of the system are the control variables and could be represented as Kaucher intervals. Furthermore, if the simulation cell is coupled to a chain of thermostats and barostats, then the positions, velocities, and forces of thermostats and barostats can also be modeled as Kaucher intervals and updated via Kaucher interval arithmetic. The advantage of this approach is that the scheme preserves the dynamics of the statistical ensemble, and therefore the uncertainty of the system can be quantified more rigorously. We refer to this scheme as the *interval statistical ensemble scheme*. The computational procedure of the interval statistical ensemble scheme is summarized in Algorithm 4.

In the NPT statistical ensemble, the simulation cell is coupled to the Nosë-Hoover chain (NHC) of thermostats and barostat. The corresponding interval governing equations of motions [25] are extended to Kaucher intervals space $\mathbb{KR}$ as

$$\left[\dot{\underline{\boldsymbol{r}}}_i, \dot{\overline{\boldsymbol{r}}}_i\right] = \frac{\left[\underline{\boldsymbol{p}}_i, \overline{\boldsymbol{p}}_i\right]}{m_i} \oplus \frac{\left[\underline{\boldsymbol{p}}_g, \overline{\boldsymbol{p}}_g\right]}{W_g} \otimes \left[\underline{\boldsymbol{r}}_i, \overline{\boldsymbol{r}}_i\right],$$

$$\left[\underline{\boldsymbol{p}}_i, \overline{\boldsymbol{p}}_i\right] = \left[\underline{\boldsymbol{F}}_i, \overline{\boldsymbol{F}}_i\right] \ominus \frac{\boldsymbol{p}_g}{W_g} \otimes \left[\underline{\boldsymbol{p}}_i, \overline{\boldsymbol{p}}_i\right] \ominus \frac{1}{N_f} \frac{\mathrm{Tr}\left[\underline{\boldsymbol{p}}_g, \overline{\boldsymbol{p}}_g\right]}{W_g} \otimes \boldsymbol{p}_i \ominus \frac{\left[\underline{p}_\xi, \overline{p}_\xi\right]}{Q} \otimes \left[\underline{\boldsymbol{p}}_i, \overline{\boldsymbol{p}}_i\right]$$

$$\left[\dot{\underline{\boldsymbol{h}}}, \dot{\overline{\boldsymbol{h}}}\right] = \frac{\left[\underline{\boldsymbol{p}}_g, \overline{\boldsymbol{p}}_g\right]}{W_g} \otimes \left[\underline{\boldsymbol{h}}, \overline{\boldsymbol{h}}\right],$$

$$\begin{aligned}\left[\dot{\underline{\boldsymbol{p}}}_g, \dot{\overline{\boldsymbol{p}}}_g\right] = {} & V\left(\left[\underline{\boldsymbol{P}}_{\mathrm{int}}, \overline{\boldsymbol{P}}_{\mathrm{int}}\right] \ominus \boldsymbol{I} P_{\mathrm{ext}}\right) \ominus \left[\underline{\boldsymbol{h}}, \overline{\boldsymbol{h}}\right] \otimes \left[\underline{\boldsymbol{\Sigma}}, \overline{\boldsymbol{\Sigma}}\right] \otimes \left[\underline{\boldsymbol{h}}^T, \overline{\boldsymbol{h}}^T\right] \\ & \oplus \left(\frac{1}{N_f} \sum_{i=1}^{N} \frac{\left[\underline{\boldsymbol{p}}_i, \overline{\boldsymbol{p}}_i\right]^2}{m_i}\right) \boldsymbol{I} \ominus \frac{\left[\underline{p}_{\xi_1}, \overline{p}_{\xi_1}\right]}{Q_1} \otimes \left[\underline{\boldsymbol{p}}_g, \overline{\boldsymbol{p}}_g\right],\end{aligned}$$

$$\left[\dot{\underline{\xi}}_k, \dot{\overline{\xi}}_k\right] = \frac{\left[\underline{p}_{\xi_k}, \overline{p}_{\xi_k}\right]}{Q_k} \quad \text{for } k = 1, \ldots, M,$$

$$\begin{aligned}\left[\dot{\underline{p}}_{\xi_1}, \dot{\overline{p}}_{\xi_1}\right] = {} & \sum_{i=1}^{N} \frac{\left[\underline{\boldsymbol{p}}_i, \overline{\boldsymbol{p}}_i\right]^2}{m_i} \oplus \frac{1}{W_g} \mathrm{Tr}\left[\left[\underline{\boldsymbol{p}}_g, \overline{\boldsymbol{p}}_g\right]^T \otimes \left[\underline{\boldsymbol{p}}_g, \overline{\boldsymbol{p}}_g\right]\right] \\ & \ominus (N_f + d^2) k T_{\mathrm{ext}} \ominus \left[\underline{p}_{\xi_1}, \overline{p}_{\xi_1}\right] \otimes \frac{\left[\underline{p}_{\xi_2}, \overline{p}_{\xi_2}\right]}{Q_2},\end{aligned}$$

$$\begin{aligned}\left[\dot{\underline{p}}_{\xi_k}, \dot{\overline{p}}_{\xi_k}\right] = {} & \left(\frac{\left[\underline{p}^2_{\xi_{k-1}}, \overline{p}^2_{\xi_{k-1}}\right]}{Q_{k-1}} \ominus k T_{\mathrm{ext}}\right) \ominus \left[\underline{p}_{\xi_k}, \overline{p}_{\xi_k}\right] \\ & \otimes \frac{\left[\underline{p}_{\xi_{k+1}}, \overline{p}_{\xi_{k+1}}\right]}{Q_{k+1}} \quad \text{for} \quad k = 2, \ldots, M-1,\end{aligned}$$

$$\left[\dot{\underline{p}}_{\xi_M}, \dot{\overline{p}}_{\xi_M}\right] = \left(\frac{\left[\underline{p}_{\xi_{M-1}}, \overline{p}_{\xi_{M-1}}\right]^2}{Q_{M-1}} \ominus k T_{\mathrm{ext}}\right), \tag{15}$$

where $\left[\underline{\boldsymbol{r}}_i, \overline{\boldsymbol{r}}_i\right]$ and $\left[\underline{\boldsymbol{p}}_i, \overline{\boldsymbol{p}}_i\right]$ are the interval positions and momentum of atom $i$, respectively, $\left[\underline{h}, \overline{h}\right]$ is the interval cell matrix, $\left[\underline{\boldsymbol{p}}_g, \overline{\boldsymbol{p}}_g\right]$ is the interval modularly invariant form of the cell momenta, $\left[\underline{\xi}_k, \overline{\xi}_k\right]$ and $\left[\underline{p}_{\xi_k}, \overline{p}_{\xi_k}\right]$ are respectively the thermostat interval variable and its conjugated interval momentum of the $k$th thermostat of the Nosë-Hoover chain of length $M$. The constant $m_i$, $W_g$, and $Q_k$ are the mass of atom $i$, barostat, and $k$th thermostat, respectively. The mass of the barostat and thermostats are used to tune the frequency where those variables fluctuate. The tensor $\boldsymbol{I}$ is the identity matrix. The constant $N_f = 3N$ is the system degrees of freedom. $T_{\mathrm{ext}}$ and $P_{\mathrm{ext}}$ denote the external temperature and external hydrostatic pressure, respectively. The matrix $\boldsymbol{\Sigma}$ is defined by

$$\boldsymbol{\Sigma} = \boldsymbol{h}_0^{-1}(\boldsymbol{t} - \boldsymbol{I} P_{\mathrm{ext}}) \boldsymbol{h}_0^{-T} \tag{16}$$

The extended interval time integration schemes are also implemented, following the time-reversible measure-preserving Verlet integrators derived by Tuckerman et al. [26].

**Algorithm 4.** Implementation of interval statistical ensemble scheme.

1: **for** every time step **do**
2: compute the total upper bound force $\overline{f}$
3: compute the total lower bound force $\underline{f}$
4: compute the total nominal force$f^*$
5: update interval velocities $[\underline{v}, \overline{v}]$ and nominal velocities $v^*$ based on the interval statistical ensemble
6: update interval positions $[\underline{x}, \overline{x}]$ and nominal positions $x^*$ based on the interval statistical ensemble
7: compute interval outputs
8: **end for**

## 4. An example of R-MD: uniaxial tensile loading of an aluminum single crystal oriented in ⟨100⟩ direction

The R-MD mechanism and four uncertainty propagating schemes are implemented on LAMMPS [20]. For each atom, the lower and upper bounds of positions, velocities, and forces, are added and retained in the computer temporary memory for every time step. Based on the interval positions, velocities, and forces, we followed the virial formula to compute the interval or radius of the microscopic symmetric pressure tensor. The implementation of the interval statistical ensemble is based on the modified C-XSC libraries [27] to include Kaucher interval arithmetic.

In the rest of this section, the simulation setting of a case study of uniaxial tensile loading of an aluminum single crystal is introduced in Section 4.1. Section 4.2 introduces the interval EAM potential for aluminum based on the error generating functions described in Section 3.3.1. Section 4.3 present the numerical results of the study. Section 4.4 compares the results of different uncertainty propagation schemes against each other. In Section 4.5, different schemes and their effectiveness are verified according to the soundness and completeness levels. In Section 4.6, the results are further verified by studying the finite-size effects of four different schemes.

### 4.1. Simulation settings

A R-MD simulation of stress-strain relation for fcc aluminum single crystal loaded in ⟨100⟩ direction [28–30] is adopted. The simulation cell contains 10 lattice constants in $x$, $y$, and $z$ directions, and 4000 atoms. The simulation time step is 1 fs, and periodic boundary condition is imposed for all directions of the simulation cell. The modified interval EAM aluminum interatomic potential used here is developed based on Mishin et al. [24], which was originally derived from both experiments and *first principles* calculations. The simulation cell is equilibrated for 20 ps, and the lattice is allowed to expand at each simulation cell boundary to a temperature of 300 K and a pressure of 0 bar. After the equilibration, all the uncertainties associated with the system control variables are reset to 0, and all the atomistic intervals are degenerated into singleton intervals. Next, the simulation cell is deformed in $x$ direction at a strain rate of $\dot{\varepsilon} = 10^{-10}$ s$^{-1}$ under the NPT ensemble. The symmetric microscopic pressure tensor is then computed as

$$P_{ij} = \frac{\sum_{k=1}^{N} m_k v_{k_i} v_{k_j}}{V} + \frac{\sum_{k=1}^{N} r_{k_i} f_{k_j}}{V} \tag{17}$$

where $m$ is the mass of the atoms, $r$, $v$, and $f$ are the atoms' positions, velocities, and interatomic forces, respectively. The pressure tensor component $P_{xx}$ is taken as the stress $\sigma$ and engineering strain values $\varepsilon$ are output into a separate file, which later is post-processed in

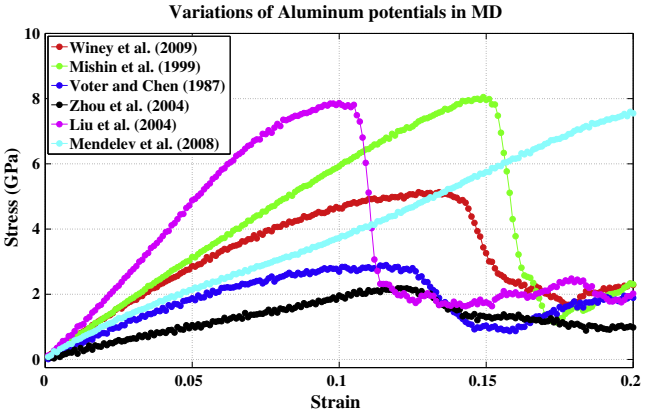


**Fig. 5.** Uniaxial tensile deformation of aluminum simulation cell using various interatomic potential.

MATLAB. As a self-consistency check, we also ran another simulation with $40 \times 40 \times 40$ lattice constants with 1 fs time step, and another $10 \times 10 \times 10$ with 0.1 fs to compare with the simulation results. Our interested quantity is the stress, which is also one the outputs of the simulation, and is directly proportional to $P_{xx}$. Thus, the goal of this case study is to quantify the uncertainty associated with the element $P_{xx}$ in the microscopic pressure tensor.

Fig. 5 presents the results of stress $\sigma = P_{xx}$ versus strain $\varepsilon$ using aluminum EAM interatomic potentials from Winey et al. [31], Mishin et al. [24], Voter and Chen [32], Zhou et al. [33], Liu et al. [34], Mendelev et al. [35]. Fig. 5 shows that the choice in potentials in MD simulation is indeed a major source of uncertainty, and demonstrates the need for quantifying uncertainty in MD potentials.

### 4.2. Interval EAM potential for aluminum based on Mishin's potential

One example of type I error generating function associated with $\rho(r)$ is shown in Fig. 6a, where $e_1(r) = ae^{-br}$, along with the sensitivity analysis results in Fig. 6b. Table 2 specifies the numerical parameters and the associated functional form to generate the uncertainty in the modified Mishin's aluminum potential [24]. An error generating function for $\rho(r)$ in the exponential form is shown in Fig. 7a, and the sensitivity analysis result is shown in Fig. 7b.

An example of type II error generating function is shown in Fig. 8a, the sensitivity of stress-strain relation because of the error is shown in Fig. 8b. The result shows that the curve is much less sensitive with respect to type II errors than to type I errors.

**Table 2**
Error generating function parameters used in the simulation sensitivity analysis.

| Function | Error type | Functional form | Parameters |
|---|---|---|---|
| Pairwise potential $\phi(r_{ij})$ | Type I | $e_1(r) = ae^{-br}$ | $a = 2.0000$, $b = 0.7675$ |
| Electron density $\rho(r)$ | Type I | $e_1(r) = ae^{-br}$ | $a = 0.0139$, $b = 0.4993$ |
| Embedding function $F(\rho)$ | Type II | $e_2(\rho) = a\left(\frac{\rho}{\rho_0}\right)^{b\rho_0} e^{-b(\rho-\rho_0)}$ | $a = 0.2700$, $b = 1.5000$ |

### 4.3. Numerical results

In this section, we concentrate on Mishin et al. [24] EAM potential, where the cutoff radius is 6.28721 Å, and study three sets of parameters for error generating functions, as tabulated in Table 3. We also set $\rho_0 = 1.0$ for all the schemes and $\alpha = 0.001$ for the total uncertainty scheme.

We compare and analyze the error qualitatively with tables and contrast the patterns of different schemes in Section 4.4. Fig. 9a shows the lower and upper bounds of pressure $P_{yy}$ using the interval statistical ensemble during the equilibration phase, with the parameters described in Table 3. Fig. 9b presents the magnified view of Fig. 9a in the window of 16–20 ps. The corresponding terms for $P_{xx}$ and $P_{zz}$ are similar to Fig. 9. As an illustration, Fig. 10a shows the interval positions of atoms as prisms at the time $t = 12$ ps within the simulation cell where the midpoints of atoms' interval positions are computed from the Verlet integrals, where the parameters from Table 2 have been used. The periodic boundary is plotted as the box. In the implementation, the interaction between particles is modeled by the extended Newton's third law as

$$[\underline{\boldsymbol{F}}_{ij}, \overline{\boldsymbol{F}}_{ij}] + [\underline{\boldsymbol{F}}_{ji}, \overline{\boldsymbol{F}}_{ji}] = 0 \tag{18}$$

or equivalently

$$\mathrm{rad}(\boldsymbol{F}_{ij}) = -\mathrm{rad}(\boldsymbol{F}_{ji}) \tag{19}$$

in Kaucher interval form, where half of the interval radii should be positive, and the other half are negative. To verify this, the radii histogram of the atom positions in $x$-direction at 12 ps is also plotted as in Fig. 10b. It shows that the mean $\mu = 2.45064 \cdot 10^{-6} \approx 0$ as expected. The distribution appears to be normal. The radii histograms of the atom position in $y$- and $z$-directions are similar to Fig. 10b.

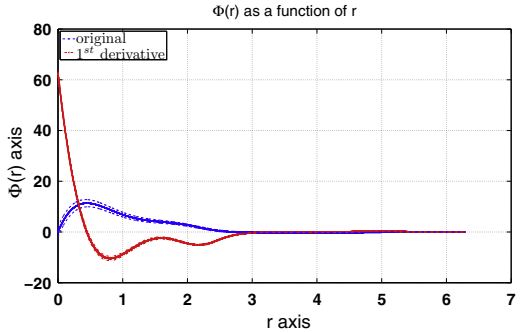


(a) Enclosed $\phi(r)$ and its first derivative by the error generating function $e_1^{(\phi)}(r_{ij})$

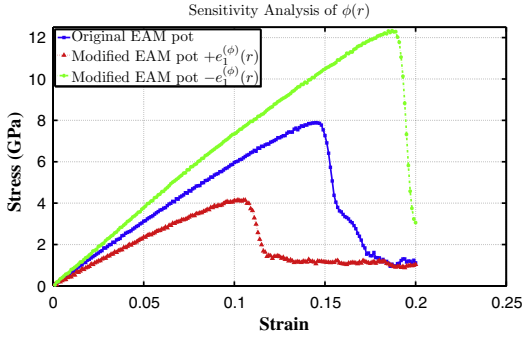


(b) The sensitivity analysis results of $\phi(r)$ with respect to the error generating function $e_1^{(\phi)}(r_{ij})$

**Fig. 6.** (a) Error generating function in $\phi(r)$ and (b) sensitivity analysis results.

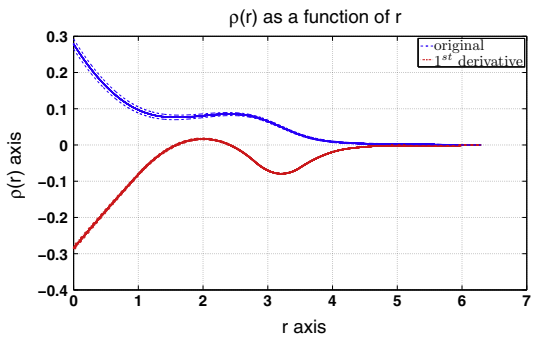


(a) Enclosed $\rho(r)$ and its first derivative by the error generating function $e_1^{(\rho)}(r_{ij})$

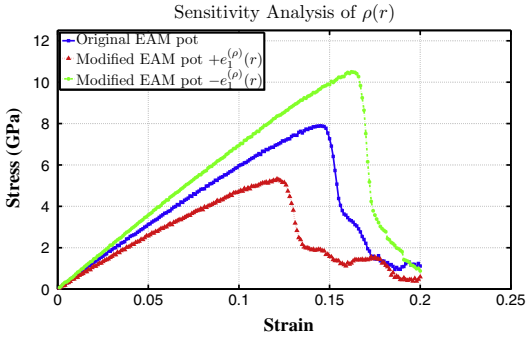


(b) The sensitivity analysis results of $\rho(r)$ with respect to the error generating function $e_1^{(\rho)}(r_{ij})$

**Fig. 7.** (a) Error generating function in $\rho(r)$ and (b) sensitivity analysis results.

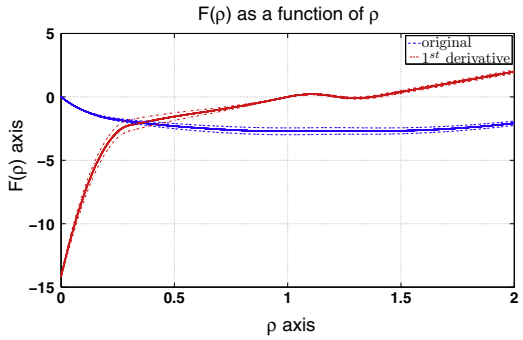


(a) Enclosed $F(\rho)$ and its first derivative by the error generating function $e_1^{(F)}(\rho)$

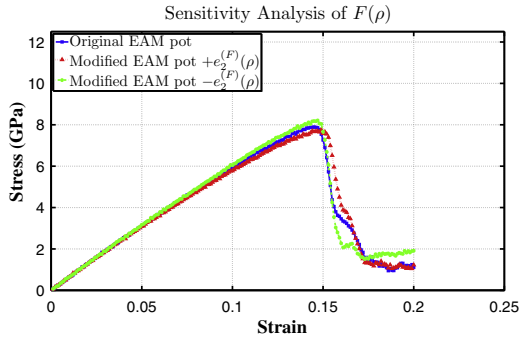


(b) The sensitivity analysis results of $F(\rho)$ with respect to the error generating function $e_1^{(F)}(\rho)$

**Fig. 8.** (a) Error generating function in $F(\rho)$ and (b) sensitivity analysis results.

**Table 3**
Error generating function parameters used in numerical study.

| $e_1^{(\phi)}(r)$ | | $e_2^{(\rho)}(r)$ | | $e_2^{(F)}(\rho)$ | |
|---|---|---|---|---|---|
| $a$ | $b$ | $a$ | $b$ | $a$ | $b$ |
| $1.2500 \cdot 10^{-2}$ | $9.2103 \cdot 10^{-1}$ | $1.3930 \cdot 10^{-4}$ | $1.2668 \cdot 10^{0}$ | $1.0800 \cdot 10^{-3}$ | $1.5000 \cdot 10^{0}$ |

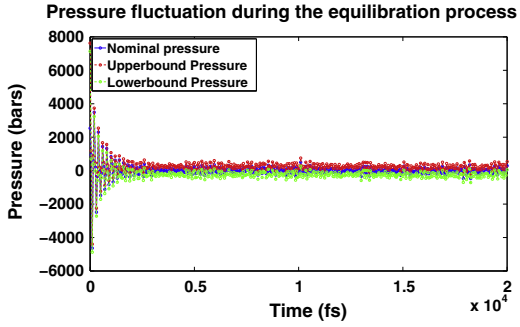


(a) Microscopic pressure $P_{yy}$ fluctuation with nominal values, lower and upper bounds during equilibration phase.

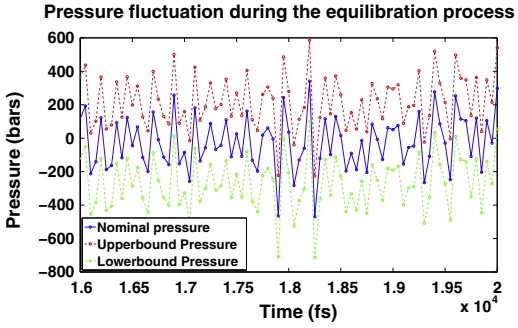


(b) Magnified view for microscopic pressure $P_{yy}$ in Figure 9a between 16ps and 20ps during equilibration phase

**Fig. 9.** Relationship between the lower bound $\underline{P_{yy}}$, the upper bound $\overline{P_{yy}}$ and the nominal $P_{yy}$ in the pressure tensor component of $y$-direction.

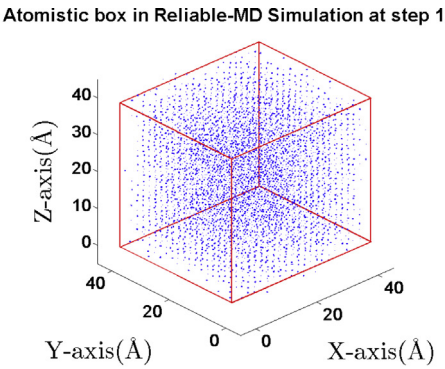


(a) Orthographic view of simulation cell in MATLAB where atoms are presented as prisms according to their interval centers and radii at time 12ps during the deformation process in the interval statistical ensemble scheme.

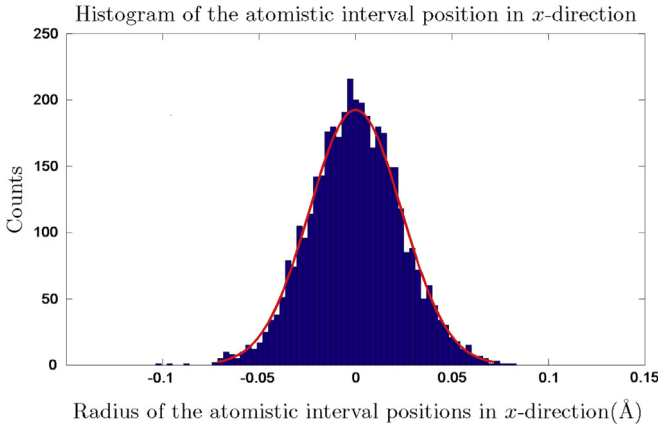


(b) Histogram of the radii of atomistic interval positions in $x$-direction in Figure 10a shows a mean very close to 0 in midpoint-radius representation scheme, illustrating Newton's third law in interval form.

**Fig. 10.** (a) Visualization of R-MD mechanism in MATLAB for interval statistical ensemble scheme and (b) the histogram of the radii of atomistic interval in $x$ direction with a normal distribution fit whose mean very close to 0.

### 4.4. Comparisons of numerical results for different schemes

To measure the deviation between the results from these four implementation schemes and those of the classical MD simulations and compare the errors between different schemes, the maximum deviation from the nominal values to the interval bounds,

$$A(\varepsilon)=\begin{cases}|\mathrm{rad}[\underline{\sigma}(\varepsilon),\overline{\sigma}(\varepsilon)]|, & \text{for midpoint-radius}\\ \max\{|\overline{\sigma}(\varepsilon)-\sigma_0(\varepsilon)|,|\underline{\sigma}(\varepsilon)-\sigma_0(\varepsilon)|\}, & \text{for lower-upper bounds}\end{cases} \tag{20}$$

is used to describe the absolute error, where $\underline{\sigma}(\varepsilon)$ is the lower bound and $\overline{\sigma}$ is the upper bound of the stress, respectively, $\sigma_0(\varepsilon)$ is the result of the classical MD simulations for the same simulation cell size. The maximum deviation $A(\varepsilon)$ is equivalent to the $l_\infty$-norm of $[\underline{\sigma},\overline{\sigma}]-\sigma_0$ in $\mathbb{R}^2$ for any $\varepsilon$ of the simulation.

Fig. 11a presents the general comparison graph among four implementation schemes, where the total uncertainty scheme is further splitted into two subschemes, one with classical intervals, and the other with Kaucher intervals. As indicated in Fig. 11a, the total uncertainty scheme with classical intervals clearly covers all the possibilities of the solutions, whereas other schemes follow very closely with the classical MD simulation result. Fig. 11b provides a magnified view of Fig. 11a, where the ranges of strain and stress are $0.0901 \leqslant \varepsilon \leqslant 0.0943$ and $5.4486 \leqslant \sigma \leqslant 5.6817$. We note that for all the schemes, the classical MD simulation result lies between the lower and upper bounds. More interestingly, for the total uncertainty scheme with Kaucher intervals, the lower and upper bounds sometimes swap the positions, but still capture the classical MD simulation solution in their ranges. This observation is contrast with the total uncertainty scheme with classical intervals, where an over-estimated solution is expected, as presented in Fig. 11a. After the plastic deformation, the result in interval statistical ensemble schemes does not follow the classical MD simulation result as closely as other non-propagating schemes, such as the midpoint-radius scheme and the lower-upper bounds scheme, but the absolute errors are comparable in the elastic portion during the deformation process. Fig. 12a shows another set of stress-strain results with larger error generating function parameters, where $e_1^{(\phi)}(r): a = 1.2500 \cdot 10^{-1}$, $b = 6.9078 \cdot 10^{-1}$; $e_2^{(\rho)}(r): a = 1.3930 \cdot 10^{-3}$, $b = 8.8305 \cdot 10^{-1}$; $e_2^{(F)}(\rho): a = 1.0800 \cdot 10^{-2}$; $b = 1.5000 \cdot 10^{0}$. Fig. 12b presents the magnified view of Fig. 12a, where the ranges of strain and stress are $0.0901 \leqslant \varepsilon \leqslant 0.0943$ and $4.900 \leqslant \sigma \leqslant 6.0000$, similar to the window of Fig. 11b for comparison purposes. The patterns of these stress-strain curves are analogous to those of Fig. 11.

Fig. 13a compares the absolute value of outer radius $A(\varepsilon)$ for the range $0 \leqslant \varepsilon \leqslant 0.1$. Fig. 13d presents the same plot, but the total uncertainty with Kaucher intervals scheme is removed to further

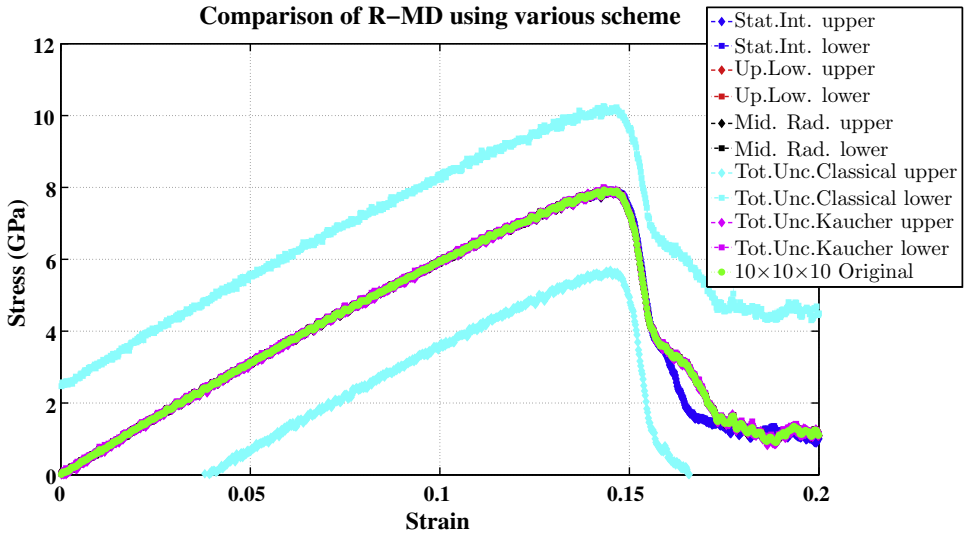


(a) General comparison between the results of all schemes showing bands with different widths covering the classical MD simulation result using parameters in Table 2.

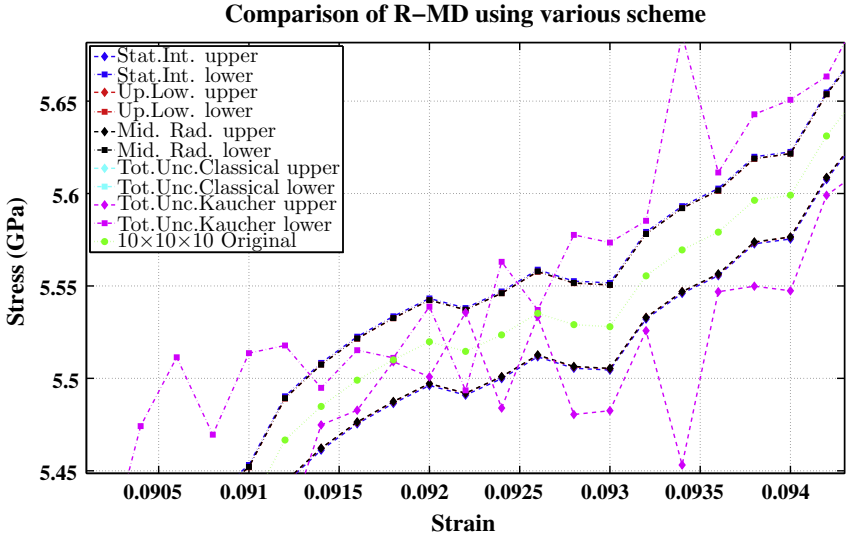


(b) Magnified view of Figure 11a where $0.0901 \leq \varepsilon \leq 0.0943$ and $5.4486 \leq \sigma \leq 5.6817$ showing the total uncertainty scheme with Kaucher intervals swap bounds during the simulation.

**Fig. 11.** Comparisons of the stress outputs computed by four different schemes. The figures show that in all implementation schemes, the classical MD simulation result is contained in the range of the implementation results.

contrast the error between the other three schemes. All of them show that the uncertainty of the simulation slightly decreases during the elastic deformation. The uncertainty in the interval statistical ensemble decreases with a slower rate, compared to the midpoint-radius and lower-upper bounds scheme. There is a good agreement between the midpoint-radius and the lower-upper bounds scheme results, because in the midpoint-radius, the midpoint of interval stress is assigned as the classical MD value, and in the lower-upper bounds scheme, the upper and lower bounds are also calculated based on the classical MD value as well. It is then expected that the uncertainty estimated by these two methods are comparable. One common feature between the midpoint-radius scheme and the interval statistical ensemble scheme is that the uncertainty does not oscillate as heavily as in the total uncertainty ensemble scheme with (Fig. 13a) and the lower-upper bounds scheme (Fig. 13d). This observation is explained by the hypothesis that compared to the non-propagating implementation schemes, the schemes that propagates the uncertainty tend to produce smoother transition between time step. Last but not least, in three schemes excluding the total uncertainty scheme, the uncertainty of the stress is predicted to grow larger after the yield point, especially in the interval statistical ensemble scheme (Fig. 13c). However, the interval statistical ensemble scheme predicts much fluctuation of the stress before the yield point (Fig. 13d), which perhaps makes more physical intuition.

Table 4 compares the computational time and slow-down factor between the different schemes to the classical MD simulation. The computational time is obtained by running the simulation with different schemes on 4 processors with MPI support. The slow-down factor is calculated the ratio of the computational time using R-MD

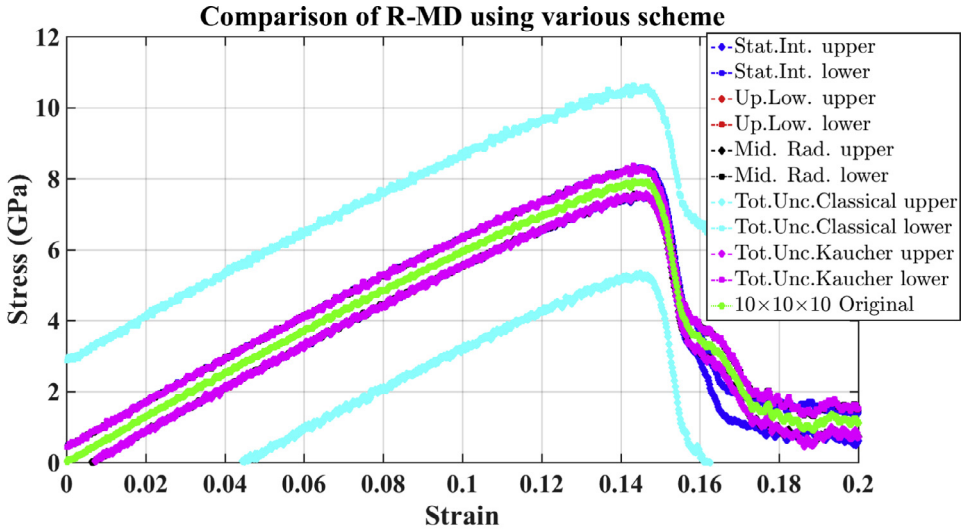


(a) Comparison between the results of all schemes showing bands with different widths covering the classical MD simulation result, with larger error generating function parameters.

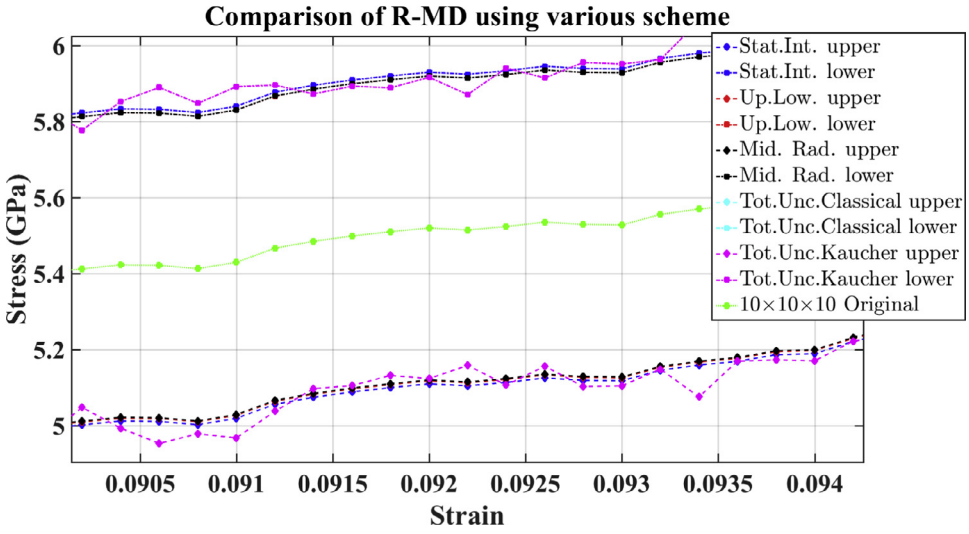


(b) Magnified view of Figure 12a where $0.0901 \leq \varepsilon \leq 0.0943$ and $4.900 \leq \sigma \leq 6.0000$.

**Fig. 12.** Comparisons of the stress outputs with larger variation, computed by four different schemes. The used parameters are $e_1^{(\phi)}(r) : a = 1.2500 \cdot 10^{-1}$, $b = 6.9078 \cdot 10^{-1}$; $e_2^{(\rho)}(r) : a = 1.3930 \cdot 10^{-3}$, $b = 8.8305 \cdot 10^{-1}$; $e_2^{(F)}(\rho) : a = 1.0800 \cdot 10^{-2}$; $b = 1.5000 \cdot 10^{0}$.

to the classical MD simulations, showing a factor of between 4 and 5 times slower compared to the classical MD simulations. This result shows the advantage of the proposed intrusive UQ method. Non-intrusive UQ techniques, such as generalized polynomial chaos expansion, and stochastic collocation, could have much more significant slow-down ratios. It demonstrates that the intrusive UQ techniques are much more computationally affordable to high-fidelity simulations, where the computational time can vary from days to months.

### 4.5. Verification and validation

We repeat the sensitivity analysis as in Figs. 6–8 in Section 3.3.1 with the error generating function parameters as tabulated in Table 3. Fig. 14a presents an overview of the four implementation results along with the sensitivity analysis results. The total uncertainty scheme with classical intervals provide a complete but also over-estimated solution. However, it does capture the variations around the yield point and after the plastic deformation. The results of sensitivity analysis is compared with the results of different schemes. We follow the soundness and completeness concepts described in Section 2. Fig. 15 explains the relationship between the estimated, the sensitive and the true range of uncertainty in UQ problem. The sensitive range, which is the solution of sensitivity analysis, is a subset of the true range. Theoretically, the true range can be obtained by Monte Carlo sampling methods. Practically, such methods are very computationally expensive and thus are not applicable. To evaluate the effectiveness of different schemes, the results obtained by R-MD are contrasted with the sensitivity analysis results using classical MD simulation with modified potentials by the error generating functions described in Section 3.3.1. A solution set is sound if it does not include an inadmissible or impossible solution; a solution set is called complete if it covers all possible solutions [36]. In Fig. 15, if the esti-

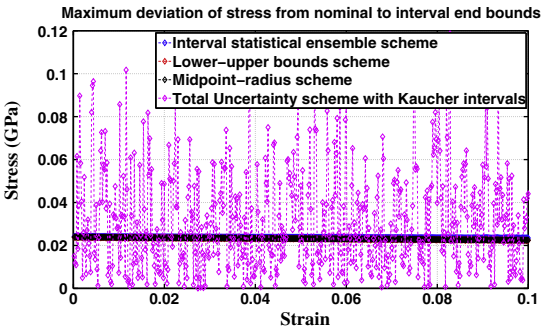


(a) $l_\infty$-norm $A(\varepsilon)$ in the four implementation schemes.

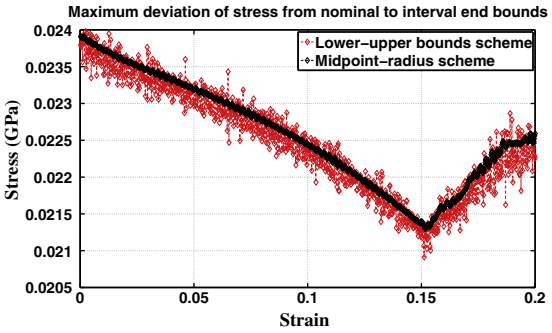


(b) $l_\infty$-norm $A(\varepsilon)$ in midpoint-radius and lower-upper bounds schemes for $0 \le \varepsilon \le 0.2$ shows an increase in stress uncertainty after the yield point.

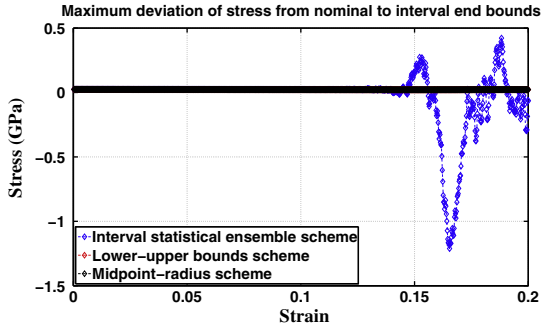


(c) $l_\infty$-norm $A(\varepsilon)$ for $0 \le \varepsilon \le 0.2$ shows a prediction of large stress uncertainty in the interval statistical ensemble scheme compared to midpoint-radius and lower-upper bounds schemes after the yield point.

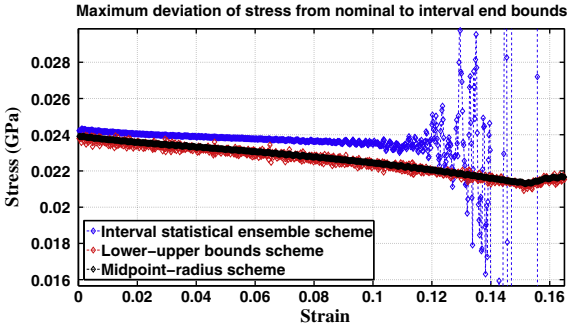


(d) $l_\infty$-norm $A(\varepsilon)$ in three schemes (excluding the total uncertainty scheme) between $0 \le \varepsilon \le 0.165$ indicates a considerable fluctuation of stress uncertainty in the interval statistical ensemble scheme before the yield point.

**Fig. 13.** Plots of $A(\varepsilon) = \max\{|\overline{\sigma} - \sigma_0|, |\underline{\sigma} - \sigma_0|\}$ in different schemes.

**Table 4**
Comparison of computational time for various schemes in R-MD.

| | Classical MD | Midpointradius | Lower-upper | Tot. uncertainty | Int. ensemble |
|---|---|---|---|---|---|
| Computational time (s) | 467.941 | 1989.812 | 1911.058 | 1932.983 | 2170.92 |
| Slow-down factor | 1 | 4.252 | 4.086 | 4.1308 | 4.639 |

mated range $X_E$ is a subset of the true range $X_T$, that is $X_E \subseteq X_T$, then $X_E$ is sound. If $X_T \subseteq X_E$, the solution set $X_E$ is complete. As intervals can also be thought of as the sets of possible solutions, the term solution set is hereby used interchangeably with the interval or the range.

In measure theory, the Lesbegue measure $\mu$ is a standard way of assigning a measure to a subsets in $\mathbb{R}^n$. For 1D, 2D and 3D, the physical meaning of Lebesgue measure is the length, the area and the volume of the set. The soundness is assigned as the ratio of Lesbegue measure of the overlapped range $X_E \cap X_T$ and the Lesbegue measure of the estimated range. Similarly, the completeness is assigned as the ratio of Lesbegue measure of the overlapped range $X_E \cap X_T$ and the Lesbegue measure of the true range.

$$\text{Soundness Index} = \frac{\mu(X_E \cap X_T)}{\mu(X_E)}, \qquad \text{Completeness Index} = \frac{\mu(X_E \cap X_T)}{\mu(X_T)} \tag{21}$$

The soundness and completeness indices are mathematically bounded between 0 and 1, as obviously $X_E \cap X_T$ is the subset of $X_E$ and $X_T$. The soundness close to 1 means the estimated solution set contains nearly all possible solutions, but also is likely to underestimate true solution set. Analogously, the completeness index close to 1 indicates a complete but over-estimated solution sets. In this case, the true solution set $X_T$ is approximated by the sensitive range $X_S$, which is defined as the smallest proper interval that contains 7 classical MD simulation results. The equivalent mathematical expression is $X_T \approx X_S$. The sensitive range $X_S$ includes 1 run with original interatomic potential and 6 other runs with modified interatomic potentials by the error generating functions, whose parameters are tabulated in Table 3. Consequently, the soundness and completeness indices are approximated as

$$\text{Soundness Index} \approx \frac{\mu(X_E \cap X_S)}{\mu(X_E)}, \qquad \text{Completeness Index} \approx \frac{\mu(X_E \cap X_S)}{\mu(X_S)} \tag{22}$$

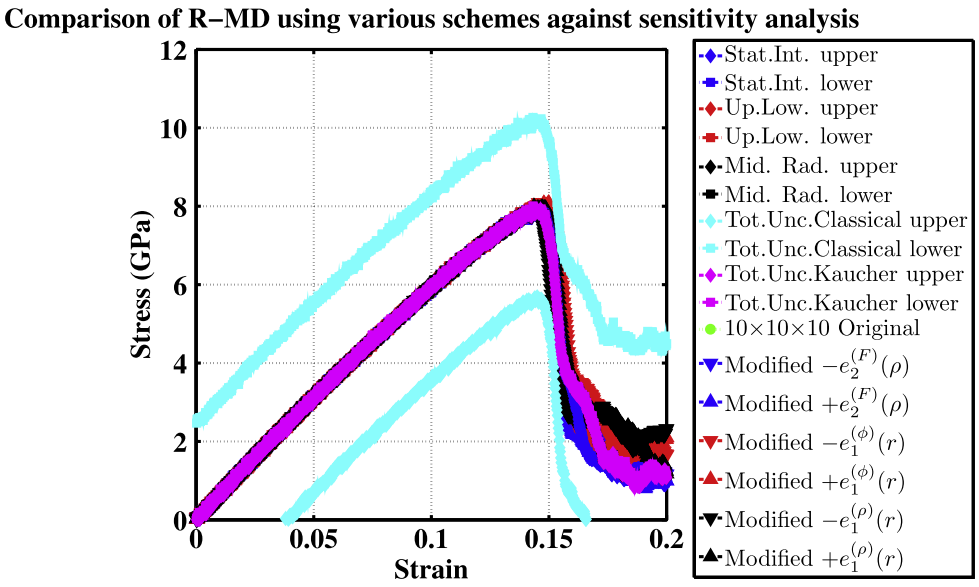


(a) Plots of sensitivity analysis and all schemes results.

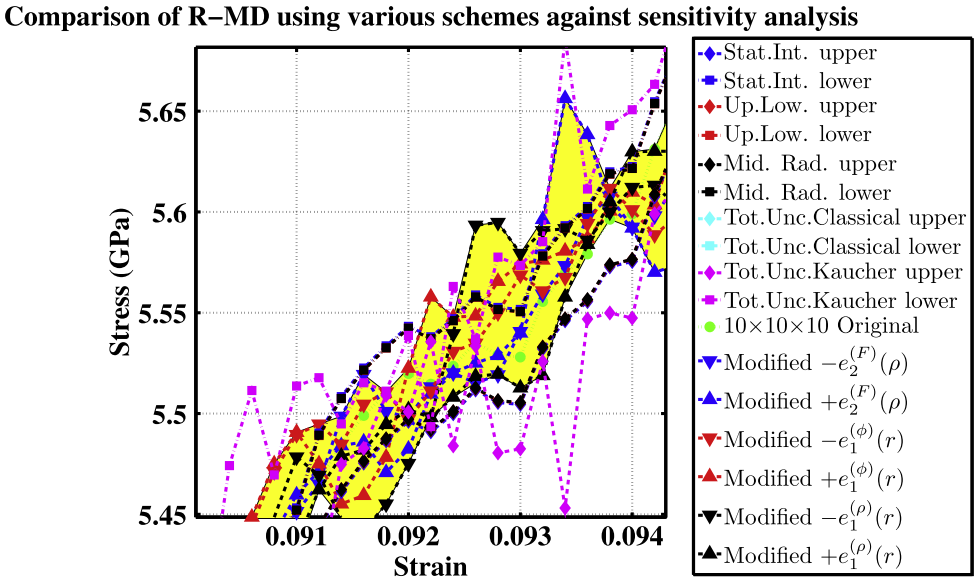


(b) Zoom-in plots of estimated stress uncertainties and sensitive stress uncertainties between $0.07 \leq \varepsilon \leq 0.075$ and $4.25 \leq \sigma \leq 4.70$. The sensitive range is filled as shaded area.

**Fig. 14.** The schematic plot and actual plot of output uncertainty. In this simulation, the sensitive range is the min and max of classical MD simulation results with the original interatomic potential and the alternated potentials by adding or subtract error generating functions to one of its three functions.

Fig. 16a and b plots the soundness and completeness of the four schemes, respectively, with the total uncertainty scheme is further divided into classical and Kaucher intervals. Fig. 16a and b also indicates that the R-MD results overlap with the sensitivity analysis. One of the differences with Section 3.3.1 sensitivity analysis is that the original result no longer always lies in the middle of the $\pm e_2^{(F)}(\rho)$, $\pm e^{(\phi)}(r)$, $\pm e^{(\rho)}(r)$ as in Section 3.3.1. Indeed, among 7 runs, the result of the classical simulation run with the original interatomic potential ends up with 10.40% getting the maximum value and 14.40% getting the minimum value in 7 values accounting for the sensitivity analysis results. The total uncertainty scheme with classical intervals achieves the completeness of 1 thoroughly during the simulation, implying that it always covers all of the true solution set. The soundness of the interval statistical ensemble scheme, along with midpoint-radius and lower-upper bounds schemes, are more consistent compared to the total uncertainty scheme. Their results represent mostly between 50% and 100% of the sensitive range. The completeness is, however, less consistent and fluctuates much, meaning they do not cover all the possibilities in the sensitive ranges, and thus will not cover all the possibilities in the true ranges as well. The total uncertainty scheme with Kaucher intervals captures the uncertainty most effectively after the deformation process, with high completeness (around 80–90% in Fig. 16b) and reasonably high soundness (30–40% in Fig. 16a).

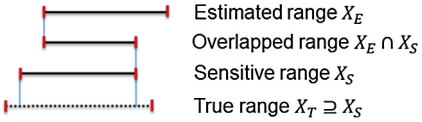


**Fig. 15.** Schematic plot of estimated, sensitive and true range of uncertainty. The sensitive range $X_S$ obtained by parametric study or sensitivity analysis is always a subset of the true range $X_T$.

Mathematically, the sensitive range is a subset of the true range, $X_S \subseteq X_T$, which also means $\mu(X_S) \leqslant \mu(X_T)$. Eqs. (21) and (22) can be manipulated algebraically further to establish the relationship

$$\frac{\mu(X_E \cap X_S)}{\mu(X_E)} \leqslant \frac{\mu(X_E \cap X_T)}{\mu(X_E)}, \tag{23}$$

and

$$\frac{\mu(X_E \cap X_S)}{\mu(X_S)} = \frac{\mu(X_E \cap X_T) - \mu(X_E \cap (X_T \setminus X_S))}{\mu(X_T) - \mu(X_T \setminus X_S)} \tag{24}$$

because of the additivity properties of Lesbegue measure on disjoint sets $X_T = X_S \cup (X_T \setminus X_S)$ and $X_S \cap (X_T \setminus X_S) = \varnothing \Rightarrow \mu(X_T) = \mu(X_S) + \mu(X_T \setminus X_S)$. Consequently, the actual soundness is expected to be higher than Fig. 16a if the true range $X_T$ is known. However, there is not enough numerical evidence to draw a conclusive comment about the completeness in Fig. 16b. The completeness could either increase or decrease depending on how $\frac{\mu(X_E \cap (X_T \setminus X_S))}{\mu(X_T \setminus X_S)}$ compares with $\frac{\mu(X_E \cap X_T)}{\mu(X_T)}$. Yet, one can be certain that if the output is not complete compared to the sensitivity analysis result, the output is also not complete compared to the true solution set.

### 4.6. Finite-size effect

We performed finite-size effect analysis for four implementation schemes with $10 \times 10 \times 10$ (4000 atoms), $12 \times 12 \times 12$ (6912 atoms), $14 \times 14 \times 14$ (10,976 atoms) and $16 \times 16 \times 16$ (16,384 atoms) lattice constants of the simulation cell with param-

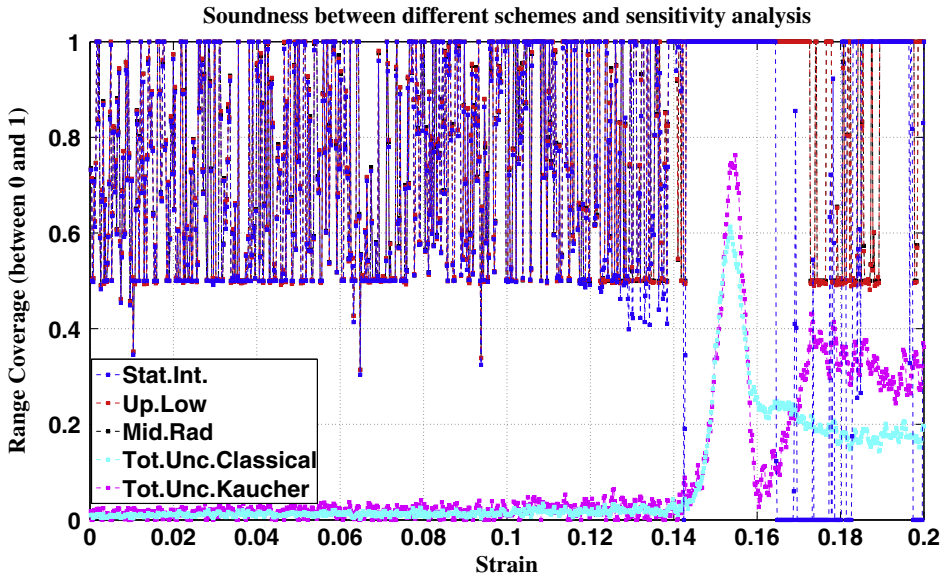


(a) Soundness indices of different uncertainty schemes.

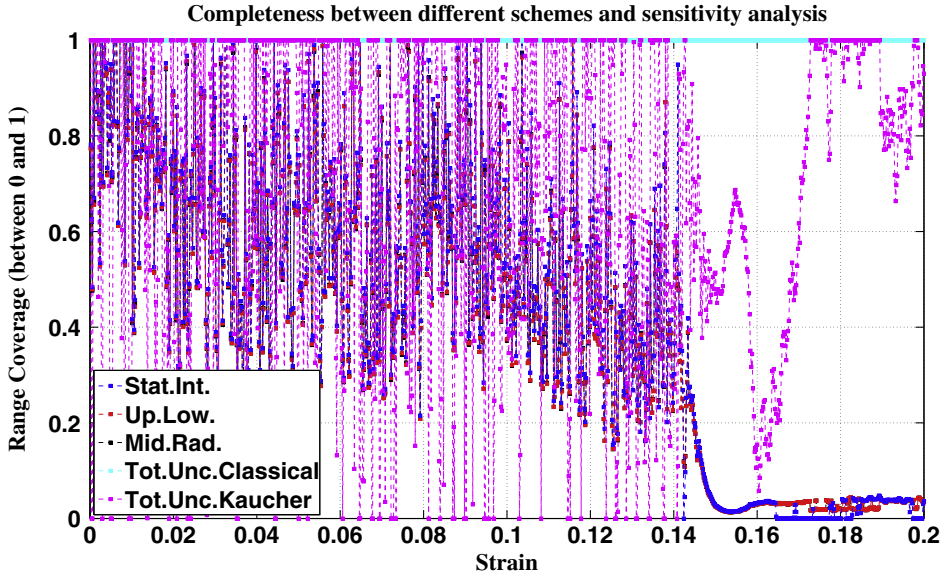


(b) Completeness indices of different uncertainty schemes.

**Fig. 16.** Comparison of soundness and completeness indices between different uncertainty schemes.

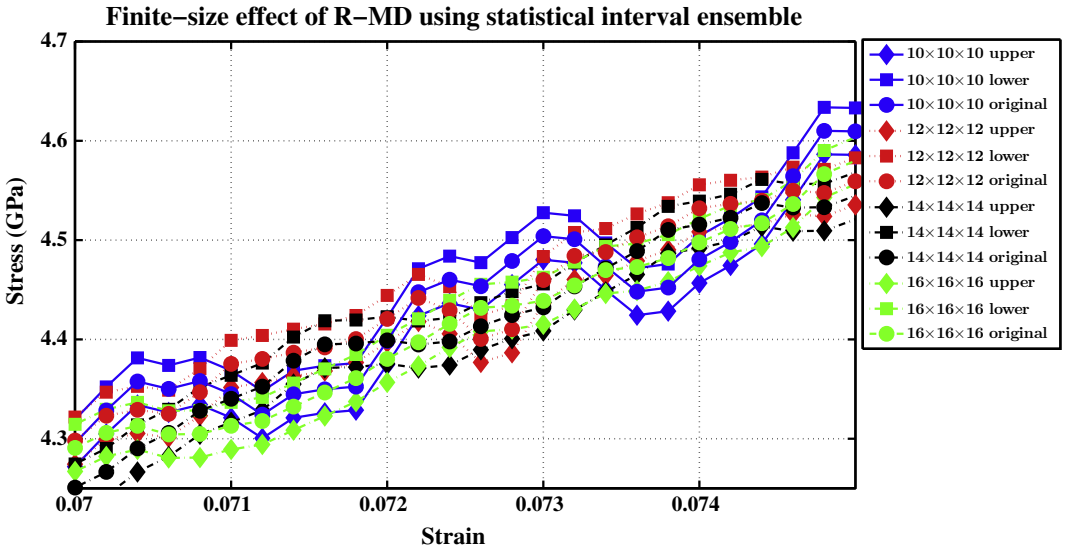


**Fig. 17.** Finite-size effect of R-MD and MD, where solid lines denote the $10 \times 10 \times 10$, dotted lines denote $12 \times 12 \times 12$, dashdot lines denote $14 \times 14 \times 14$, dashed lines denote $16 \times 16 \times 16$.

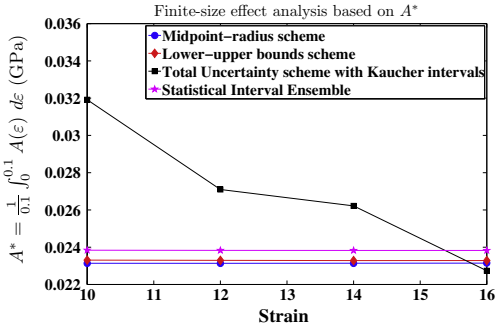


**Fig. 18.** Error analysis of $A^*$ for different schemes with respect to different sizes of the simulation cell.

eters as in Table 3. The results of R-MD are then compared with the results of the classical MD simulations with the corresponding size of $10 \times 10 \times 10$, $12 \times 12 \times 12$, $14 \times 14 \times 14$ and $16 \times 16 \times 16$. Fig. 17 presents magnified view of the finite-size effect of the interval statistical ensemble between $0.07 \leqslant \varepsilon \leqslant 0.075$ and $4.25 \leqslant \sigma \leqslant 4.70$. The solid lines denote the $10 \times 10 \times 10$, the dotted lines denote $12 \times 12 \times 12$, dashdot lines denote $14 \times 14 \times 14$, dashed lines denote $16 \times 16 \times 16$ simulation results. Also, on the same graph, the diamond markers denote the upper bound, the square makers denote the lower bound and the circles denote the classical MD simulation results.

To measure the convergent of different uncertainty quantification schemes, the strain-averaged absolute stress error between $0 \leqslant \varepsilon \leqslant 0.1$, denote as $A^*$,

$$A^* = \frac{1}{0.1}\int_0^{0.1} A(\varepsilon) d\varepsilon \tag{25}$$

where $A(\varepsilon)$ is the maximum deviation from the nominal to the interval end bounds in Eq. (20) because of the input uncertainty in the interatomic potential, is used to verify the finite-size effect of different schemes. The reason that $\varepsilon = 0.1$ is picked as the upper bound of the integral is that after the simulation cell runs into plastic deformation, it is hard to quantify and predict the error exactly, and between the range $[0, 0.1]$ the stress $\sigma$ versus strain $\varepsilon$ curves are more consistent so that they can be compared qualitative against each other. Mathematically, $A^*$ is proportional to the $L_1$-norm of $A(\varepsilon)$ because $A(\varepsilon)$ measures how far the interval bounds is compared to the nominal values. Concisely, $A^*$ is a compound $L_1 \circ l_\infty$-norms to qualitative describe the finite-size effect of the simulation results. We expect other compound norms of the same kind, that is, $L_p \circ l_q$-norms, to behave similarly, and thus, the quantity $A^*$ can be justified as an arbitrary measure for the finite-size effects. The value of $A^*$ is obtained by integrating the $A(\varepsilon)$ numerically by trapezoidal rule. Fig. 18 presents the integral strain-averaged absolute stress error $A^*$ with respect to different sizes of the simulation cell, showing a convergent error with respect to the size of simulation cells for all the schemes. The total uncertainty scheme with Kaucher intervals has one more parameter $\alpha$ to model the temperature measurement at every time step, thus it is not expected to exactly follow other schemes. However, the total uncertainty scheme with Kaucher interval still shows a convergent pattern with respect to the increase size in the simulation cell. We then conclude all four implementation schemes yield reliable results.

## 5. Discussion

There are different advantages and disadvantages between intrusive and non-intrusive techniques that one should consider before applying any of these methods. Disadvantages in intrusive UQ techniques are as follows. Simulator is required to be modifiable. Analysts need to have comprehensive understanding of how to apply intrusive UQ techniques to that simulator. Extra time is also needed to develop UQ solution. However, these drawbacks can be mitigated by introducing an open framework or application program interfaces in simulation packages by developers to assist the analysts. The main advantages of intrusive UQ techniques are their ability to estimate the variation ranges of outputs (via interval analysis) or the probability density function itself (via intrusive polynomial chaos expansion) without sampling inputs and repeating the simulation. The simulator developers and UQ analysts can work together to have UQ embedded in simulator so that the detailed knowledge of UQ is not required as the user of simulator. On the other hand, disadvantages of non-intrusive UQ techniques are as follows. First, simulation needs to be repeated throughout the input parameter space, even though this problem can be alleviated by using sparse grids. Second, there are many cases where

the input parameters of simulation are functions. Capturing uncertainty associated with these functions is still a challenge to non-intrusive UQ techniques. The advantages of non-intrusive UQ include the possibility of building a computationally efficient surrogate model or a meta-model of simulations so that the output can be quickly evaluated. It also allows to capture the output probability density function in details. Non-intrusive UQ techniques can be developed as independent packages to couple with any simulations.

The interval UQ technique is an intrusive and non-probabilistic that promptly provides the range estimation for the bounds of output probability density function with only one or two runs. For the algorithm with midpoint-radius representation, the output result is an interval radius, of which midpoint is identical with classical MD simulation. With the choice of inner or outer radius, the results will be different, and therefore two runs are recommended. One run is with the inner radius for all atomistic positions, velocities, and forces, whereas another run is with outer radius. Between both of them, the choice of inner radius provides higher soundness, but lower completeness, compared to the choice of outer radius. For the algorithm with lower-upper bounds representation, the output result is an interval which contains the quantified uncertainty information, and thus only one run is needed in this case. Between two interval representations, the lower-upper bounds representation is superior to the midpoint-radius representation, because the former only requires one run, based on the fact that two bounds are computed simultaneously. Additionally, all of the interval Kaucher arithmetic computations are carried out based on the lower-upper bounds representation as in Lakeyev's formula and Kaucher multiplication table, which are described in Section 2. Therefore, the lower-upper bounds representation saves computational time compared to midpoint-radius representation.

Beside the low number of runs needed to obtain a UQ solution, the interval technique also allows to capture and incorporate the uncertainty associated with the input potential functions into simulation, by modeling the error generating function. In this study, two forms of analytical error generating function are proposed. Other forms of error generating functions can also be similarly implemented. Even though not considered in this study, the interval technique can also be applied to capture aleatory uncertainty associated with thermal fluctuation. For example, the aleatory uncertainty of Langevin thermostat can be quantified by interval-valued atomistic force, velocity, and position to solve the stochastic differential equations. By quantifying the uncertainty internally, the intrusive UQ method offers an efficient way to assess sensitivity without sampling. The interval approach can be viewed as an efficient alternative technique to sampling-based sensitivity analysis where variation ranges are estimated. However, if the complete information of probability density functions is required, one should resort to the probabilistic approaches.

As the simulation schemes change, new intrusive UQ solutions are required to be developed to adapt with the changes in simulation. During this study, we have implemented and provided a basic platform that can be extended to general intrusive UQ solutions in LAMMPS package. Still, there is a bargaining trade-off between the time invested to develop an intrusive UQ solution and the time spent on repetitive simulations for non-intrusive UQ techniques. Another limitation of the interval technique at the current stage is its inability to quantify output probabilistically, such as joint density, correlations, and moments. A more advanced concept that fuses both interval and statistical method is probability bounds analysis [37] that envelops the cumulative density function by using interval methods. Based on the uncertain cumulative density function, one can derive the uncertain probability density function, and thus other statistical quantities. In addition, quantifications of correlation between intervals [38] and between random sets [39] have been studied to assess interdependency similarly to the probabilistic approach. These issues remain as open questions for future research.

The classical interval has been shown to be a conservative choice, in the sense that it almost always produces a complete but over-estimated range. Therefore, the Kaucher intervals are used as a substitute an extension because of better algebraic properties. The Kaucher interval arithmetic yields a much smaller epistemic uncertainty compared to the classical interval arithmetic by the introduction of improper intervals, and hence tends to reduce much the impact of over-estimation and self-dependency problem in classical intervals, and perhaps keep the epistemic uncertainty within some acceptable bounds. For MD simulation with EAM potential functions, the Kaucher interval technique is considerably efficient in term of computational time, because this methodology does not require the simulation to repeat numerous times. In our study, the computational time is between 4.1 and 4.6 times more than the classical MD simulations, which is an important improvement in term of computational time.

One of the criteria to evaluate the effectiveness of a UQ solution is to compare the estimated uncertainties with the true ones. If the estimated uncertainty is considerably greater compared to the true uncertainty, the solution does not hold much valuable, meaningful or conclusive information. For output with probability density function, such as polynomial chaos expansion, Monte Carlo, and Latin hypercube sampling methods, one can, for example, measure the distance between two distributions by any $L^p$ norm, or Kullback–Leibler divergence. For output with range or probability density function bounded support estimation, represented as intervals, one can compare the estimate interval with the true interval derived from any sampling methods. The effectiveness of interval UQ method is then quantified by soundness and completeness indices, which are bounded between 0 and 1. Physically, these indices measure the ratios of the width of the "shared" interval to the width of estimated and true intervals. Since the true interval is not available, we approximate the true interval by finite sampling runs with alternated potentials. The approximated soundness and completeness indices are then compared to the true one by algebraic relations. For the uniaxial tensile of aluminum single crystal example with NPT ensemble in this study, the UQ solution are shown to be more sound and complete during the elastic deformation regime than the plastic deformation regime.

So far, we have considered the uncertainty of the force by computing the *total* lower and upper bounds interval force separately. Another way to compute the force uncertainty is to consider its contribution from each *individual* pairs. This scheme has also been attempted in the study, and the same issue for this implementation scheme is that the temperature uncertainty is very large, even compared to the total uncertainty scheme with classical intervals. The same treatment for temperature is also applied, that is, the uncertainty of pressure is only calculated by the interval force and interval position term, but not the kinetic term. Still, the epistemic uncertainty are too large to declare a meaningful approach for the UQ problem. In fact, the pressure UQ problem with constraint on the temperature uncertainty in this case study is a special case of another more general problem, which is a UQ problem with *uncertainty constraint* on related quantities.

Four different implementation schemes have been developed to quantify the uncertainty in MD simulations. The total uncertainty scheme with classical intervals produces the most conservative, yet over-estimated results, as expected. The total uncertainty scheme with Kaucher intervals is less conservative, and follows more closely with the interval statistical ensemble and other results. The $\alpha$ parameter is set to 0.001 through trials and errors. Reducing this $\alpha$ parameters will also reduce the width of the interval stress. Perhaps the most interesting findings in these sim-

ulation runs is that the uncertainty does not always grow larger. Indeed, it becomes smaller toward the yield point. However, only in the interval statistical ensemble, the stress uncertainty heavily fluctuates after the yield point. In our opinion, this behavior truly reflects the simulation uncertainty because in the interval statistical ensemble, the system dynamics is preserved from the beginning to the end of the simulation. Therefore, the interval statistical ensemble is recommended for the propagating schemes. Regarding the completeness and soundness of the interval statistical ensemble, the interval stress is fairly sound, based on the fact that its estimated range provides at least 50% of the true solution set (Fig. 16a). Yet, it is not complete, but also covers around 50% of the true solutions on average (Fig. 16b). For non-propagating schemes, the total uncertainty schemes with classical intervals is recommended, because it demonstrates the worst-case scenario. For most of the deformation process, this level of conservative yields a very low soundness on the solution. However, right after the yield point deformation process, it represents almost 60% of the solution set (Fig. 16a). If one is concerned with the behavior of the stress right after the peak, then the total uncertainty scheme is suggested. The completeness of the total uncertainty scheme with classical intervals is uniformly 1, implying that it always covers more than all possibilities.

## 6. Conclusions

In this paper, we introduce a novel concept of MD that uses interval analysis to quantify the uncertainty in MD simulation. The uncertainty in tabulated EAM potential is captured by analytical forms of error generating functions. Based on the uncertainty of the inputs, four different implementation schemes are proposed and developed to quantify the uncertainty of the simulation. Among these four schemes, the total uncertainty and the lower-upper bounds are non-propagating, and the midpoint-radius scheme and the interval statistical ensemble are propagating schemes. For non-propagating schemes, at every time step, the uncertainty of the simulation system is estimated, but not carried forward to quantify the uncertainty at the next time step. The physical interpretation is that these non-propagating schemes compute the uncertainty of the output due to the uncertainty of the interatomic potentials at every time step. For propagating schemes, the uncertainty of the simulation system is quantified and propagated toward the end of the simulation. The midpoint-radius scheme and total uncertainty scheme utilizes the midpoint-radius representation of intervals, whereas the lower-upper bound scheme and the interval statistical ensemble scheme use the lower-upper bounds representation of intervals. In the non-propagating schemes, such as lower-upper bounds and total uncertainty schemes, the oscillations of uncertainty are expected. At different time steps in these non-propagating schemes, the uncertainty of the system is quantified by the interval force, which originally comes from the interatomic potentials uncertainty. Because the uncertainty does not propagate from the previous time step to the current time step, it fluctuates more heavily compared to that of propagating schemes. In propagating schemes, such as interval statistical ensemble and midpoint-radius schemes, the uncertainty propagates from the beginning of the simulation to the end. Based on the findings in this work, the interval statistical ensemble is recommended for investigating the uncertainty qualitatively and quantitatively, because it preserves the simulation dynamics and only generalizes the real number to intervals. On the other hand, the total uncertainty scheme with classical intervals is also recommended due to their completeness. Even though the estimated solution range are over-estimated most of the time, this scheme can be very useful during critical events (the yield point in this case). However, one should process with caution respect to the $\alpha$ parameter. In this study, $\alpha$ was tuned to 0.001 mostly by trials and errors. The advantage of R-MD is that the uncertainty can be quantified based on one or two runs of the simulations, compared to hundreds or thousands runs of other non-intrusive UQ techniques. The experience, along with the results found in this paper, shows that the interval statistical ensemble is the most promising direction to quantify and propagate the uncertainty. Further work will include the implementation of more interval interatomic potential such as Lennard-Jones, Stillinger-Weber, and others.

## Acknowledgement

The project is supported in part by U.S. National Science Foundation under Grant No. CMMI-1306996. The first author thanks Werner Hofschuster at University of Wuppertal for many helpful conversations about C-XSC interval libraries. The authors also thank two anonymous reviewers for their valuable suggestions during the review process to improve the paper.

## References

[1] R.G. Ghanem, P.D. Spanos, Stochastic Finite Elements: A Spectral Approach, Courier Corporation, 2003.
[2] G.A. Pavliotis, Stochastic processes and applications: Diffusion Pro-cesses, the Fokker-Planck and Langevin Equations, Springer, 2014.
[3] E.K. Gross, R.M. Dreizler, Density Functional Theory, vol. 337, Springer Science & Business Media, 2013.
[4] A. Chernatynskiy, S.R. Phillpot, R. LeSar, Uncertainty quantification in multiscale simulation of materials: a prospective, Ann. Rev. Mater. Res. 43 (2013) 157–182.
[5] Y. Wang, Uncertainty in materials modeling, simulation, and development for ICME, in: Proceedings of the 2015 Materials Science and Technology, 2015.
[6] S.L. Frederiksen, K.W. Jacobsen, K.S. Brown, J.P. Sethna, Bayesian ensemble approach to error estimation of interatomic potentials, Phys. Rev. Lett. 93 (16) (2004) 165501.
[7] L.C. Jacobson, R.M. Kirby, V. Molinero, How short is too short for the interactions of a water potential? Exploring the parameter space of a coarse-grained water model using uncertainty quantification, J. Phys. Chem. B 118 (28) (2014) 8190–8202.
[8] F. Cailliez, P. Pernot, Statistical approaches to forcefield calibration and prediction uncertainty in molecular simulation, J. Chem. Phys. 134 (5) (2011) 054124.
[9] F. Rizzi, H. Najm, B. Debusschere, K. Sargsyan, M. Salloum, H. Adalsteinsson, O. Knio, Uncertainty quantification in MD simulations. Part I: forward propagation, Multisc. Model. Simul. 10 (4) (2012) 1428.
[10] F. Rizzi, H. Najm, B. Debusschere, K. Sargsyan, M. Salloum, H. Adalsteinsson, O. Knio, Uncertainty quantification in MD simulations. Part II: Bayesian inference of force-field parameters, Multisc. Model. Simul. 10 (4) (2012) 1460.
[11] P. Angelikopoulos, C. Papadimitriou, P. Koumoutsakos, Data driven, predictive molecular dynamics for nanoscale flow simulations under uncertainty, J. Phys. Chem. B 117 (47) (2013) 14808–14816.
[12] F. Cailliez, A. Bourasseau, P. Pernot, Calibration of forcefields for molecular simulation: sequential design of computer experiments for building cost-efficient kriging metamodels, J. Comput. Chem. 35 (2) (2014) 130–149.
[13] M. Wen, S. Whalen, R. Elliott, E. Tadmor, Interpolation effects in tabulated interatomic potentials, Model. Simul. Mater. Sci. Eng. 23 (7) (2015) 074008.
[14] M. Hunt, B. Haley, M. McLennan, M. Koslowski, J. Murthy, A. Strachan, PUQ: a code for non-intrusive uncertainty propagation in computer simulations, Comp. Phys. Commun. 194 (2015) 97–107.
[15] G. Li, C. Rosenthal, H. Rabitz, High dimensional model representations, J. Phys. Chem. A 105 (33) (2001) 7765–7777.
[16] A.V. Tran, Y. Wang, A molecular dynamics simulation mechanism with imprecise interatomic potentials, in: Proceedings of the 3rd World Congress on Integrated Computational Materials Engineering (ICME), John Wiley & Sons, 2015, p. 131.
[17] A.V. Tran, Y. Wang, Quantifying model-form uncertainty in molecular dynamics simulation, TMS 2016 Supplemental Proceedings (2016) 283.
[18] E. Kaucher, Interval analysis in the extended interval space $\mathbb{IR}$, in: Fundamentals of Numerical Computation (Computer-Oriented Numerical Analysis), Springer, 1980, pp. 33–49.
[19] R.E. Moore, R.B. Kearfott, M.J. Cloud, Introduction to Interval Analysis, SIAM, 2009.
[20] S. Plimpton, Fast parallel algorithms for short-range molecular dynamics, J. Comput. Phys. 117 (1) (1995) 1–19.
[21] A. Lakeyev, Linear algebraic equations in Kaucher arithmetic, Reliab. Comput. (1995) 23–25.

[22] M.S. Daw, M.I. Baskes, Embedded-atom method: derivation and application to impurities, surfaces, and other defects in metals, Phys. Rev. B 29 (12) (1984) 6443.
[23] M.S. Daw, S.M. Foiles, M.I. Baskes, The embedded-atom method: a review of theory and applications, Mater. Sci. Rep. 9 (7) (1993) 251–310.
[24] Y. Mishin, D. Farkas, M.J. Mehl, D.A. Papaconstantopoulos, Interatomic potentials for monoatomic metals from experimental data and ab initio calculations, Phys. Rev. B 59 (1999) 3393–3407, http://dx.doi.org/10.1103/PhysRevB.59.3393. <http://link.aps.org/doi/10.1103/PhysRevB.59.3393>.
[25] W. Shinoda, M. Shiga, M. Mikami, Rapid estimation of elastic constants by molecular dynamics simulation under constant stress, Phys. Rev. B 69 (13) (2004) 134103.
[26] M. Tuckerman, B.J. Berne, G.J. Martyna, Reversible multiple time scale molecular dynamics, J. Chem. Phys. 97 (3) (1992) 1990–2001.
[27] R. Klatte, U. Kulisch, A. Wiethoff, M. Rauch, C-XSC: A C++ Class Library for Extended Scientific Computing, Springer Science & Business Media, 2012.
[28] D.E. Spearot, M.A. Tschopp, K.I. Jacob, D.L. McDowell, Tensile strength of ⟨1 0 0⟩ and ⟨1 1 0⟩ tilt bicrystal copper interfaces, Acta Mater. 55 (2) (2007) 705–714.
[29] M. Tschopp, D. Spearot, D. McDowell, Atomistic simulations of homogeneous dislocation nucleation in single crystal copper, Model. Simul. Mater. Sci. Eng. 15 (7) (2007) 693.
[30] M. Tschopp, D. McDowell, Influence of single crystal orientation on homogeneous dislocation nucleation under uniaxial loading, J. Mech. Phys. Solids 56 (5) (2008) 1806–1830.
[31] J. Winey, A. Kubota, Y. Gupta, A thermodynamic approach to determine accurate potentials for molecular dynamics simulations: thermoelastic response of aluminum, Model. Simul. Mater. Sci. Eng. 17 (5) (2009) 055004.
[32] A.F. Voter, S.P. Chen, Accurate interatomic potentials for ni, al and ni3al, MRS Proceedings, vol. 82, Cambridge Univ Press, 1986, p. 175.
[33] X. Zhou, R. Johnson, H. Wadley, Misfit-energy-increasing dislocations in vapor-deposited cofe/nife multilayers, Phys. Rev. B 69 (14) (2004) 144113.
[34] X.-Y. Liu, F. Ercolessi, J.B. Adams, Aluminium interatomic potential from density functional theory calculations with improved stacking fault energy, Model. Simul. Mater. Sci. Eng. 12 (4) (2004) 665.
[35] M. Mendelev, M. Kramer, C. Becker, M. Asta, Analysis of semi-empirical interatomic potentials appropriate for simulation of crystalline and liquid Al and Cu, Philos. Magaz. 88 (12) (2008) 1723–1750.
[36] Y. Wang, Solving interval master equation in simulation of jump processes under uncertainties, in: ASME 2013 International Design Engineering Technical Conferences and Computers and Information in Engineering Conference, American Society of Mechanical Engineers, 2013.
[37] S. Ferson, R.B. Nelsen, J. Hajagos, D.J. Berleant, J. Zhang, W.T. Tucker, L.R. Ginzburg, W.L. Oberkampf, Dependence in Probabilistic Modeling, Dempster–Shafer Theory, and Probability Bounds Analysis, Sandia National Laboratories, Report No. SAND2004-3072.
[38] S. Ferson, V. Kreinovich, Modeling correlation and dependence among intervals, NSF Workshop Reliable Eng. Comput. (2006) 115–126.
[39] F. Tonon, C.L. Pettit, Toward a definition and understanding of correlation for variables constrained by random relations, Int. J. Gen. Syst. 39 (6) (2010) 577–604.